

# Autonomous Space Navigation Using X-ray Horizon Crossings

Nathaniel C. Ruhl

Advised by Andrea N. Lommen  
Department of Physics and Astronomy  
Haverford College  
May, 2022

## Abstract

The Horizon Crossing Navigational Method (HCNM) is a method of autonomous, celestial-based X-ray navigation in which an X-ray source is observed by a telescope aboard a satellite. HCNM can be used to determine highly accurate in-track navigational information whenever navigating around a planet with a known atmospheric model. In Part I of this paper, the concepts behind HCNM are presented by solving a variation of the cold start problem, or a “cool start” problem, for a circular orbit. Unlike the “cold start” problem in which nothing is known about a spacecraft’s trajectory before attempting to determine its position, in the cool start problem, a few parameters are known about the spacecraft’s orbit, such as the size of the orbited planet and the planet’s atmosphere. By analyzing 1.0 – 5.0 keV X-rays emitted from the black hole binary candidate V4641 Sagitarii, as collected by the Neutron Star Interior Composition Explorer (NICER) telescope on the International Space Station (ISS), the position of the ISS is located to an average of 2.6 km over four energy bands, while the in-track position is located to an accuracy of less than 1.0 km. In the case where Earth is approximated as a sphere, the the in-track position is only accurate to 10.4 km.

In Part II, the performance of HCNM is considered when there is uncertainty in the input orbital model, as well as uncertainty in the planet’s atmospheric model. Directions for future research and simulations are discussed in order to better understand the “error budget” of HCNM and how it can be used for deep space navigation. HCNM has the potential provide highly-accurate in-track measurements that can enhance the performance of an autonomous X-ray navigation system, such as X-ray Pulsar Navigation (XNAV). The consolidation of these two methods in a navigational filter will be extremely important as we navigate around planets in the outermost parts of our Solar System and beyond.



**HAVERFORD**  
COLLEGE

---

## Dedication

To mom and dad. Thank you for helping me become the person I am today. Without your unwavering support, I would not have gotten to this point.

## Acknowledgements

Thank you to Andrea N. Lommen for advising and supporting me throughout this project. I would like to thank Kent S. Wood for all of his guidance during this project. Thank you for trusting me to develop some of your ideas about horizon crossings that originated at the Naval Research Laboratory. Paul S. Ray has provided helpful information and support throughout this project. Thank you to Zaven Arzoumanian and Keith C. Gendreau for supporting our research of horizon crossings. Thanks to the rest of the NICER Pulsar Timing group for providing input and feedback on this project.

Satoru Katsuda and Teru Enoto have provided helpful discussions about horizon crossing analysis. Thank you to Suneel I. Sheikh, Kevin D. Anderson, and Campbell T.L. Dunham for their efforts to integrate HCNM into the navigational filter at ASTER Labs. Thank you to Noah H. Schwab, Romana M. Hladky, Avi Patel, and Fatima Irfan for their work on Horizon Crossings at Haverford College.



## Permissions

All Figures in this paper are original except three. Figure 1.3 is reprinted from Wood and Ray (2017) with permission from the author. Figure 5.1 is from the online course website of a Penn State University course: <https://www.e-education.psu.edu/geog862/book/export/html/1669>. Figure 3.5 is reprinted from the textbook “Orbital Mechanics for Engineering Students” by Howard D. Curtis, Copyright Elsevier, 2005.

## Code

All code is available upon request.

## Contents

<b>List of Figures</b>	<b>iv</b>
<b>List of Tables</b>	<b>vi</b>
<b>1 Introduction</b>	<b>1</b>
1.1 Current Methods of Deep Space Navigation . . . . .	1
1.2 Introduction to Horizon Crossings . . . . .	1
1.3 History of X-ray Navigation . . . . .	5
1.4 The Vision of X-ray Navigation . . . . .	7
1.5 Dual Use of X-ray Horizon Crossings . . . . .	9
1.6 NICER Specifications . . . . .	9
<b>Part I: HCNM and the “Cool Start” Scenario</b>	<b>11</b>
<b>2 Formulation of the Navigational Problem</b>	<b>11</b>
<b>3 Geometry of a Horizon Crossing</b>	<b>12</b>
3.1 Two-Dimensional HC Geometry . . . . .	12
3.1.1 Position of Satellite at Crossing: a Two-Dimensional View . . . . .	12
3.2 Three-Dimensional Geometry . . . . .	15
3.2.1 Position of Satellite at Crossing: a Three-Dimensional View . . . . .	16
<b>4 Atmospheric Model</b>	<b>18</b>
<b>5 Application to the ISS orbit</b>	<b>19</b>
5.1 Atmospheric Model of Earth . . . . .	19
5.2 Oblate Model of Earth . . . . .	20
5.3 The Navigational Method . . . . .	21
5.3.1 Calculating Orbital Period . . . . .	21
5.3.2 Locating the Position of the ISS at Crossing . . . . .	22
5.3.3 Identifying the Time of Crossing . . . . .	23
5.4 Reference Position of the ISS at Crossing . . . . .	27
5.5 Results and Error Analysis . . . . .	27
5.5.1 Note on Error Analysis . . . . .	27
5.5.2 Oblate Earth Model . . . . .	28
5.5.3 Navigational Scenario: Spherical Earth Approximation . . . . .	33
5.5.4 Weighted Mean of Results . . . . .	34
<b>Part II: Simulations and Error Budget of HCNM</b>	<b>36</b>
<b>6 Two NICER Horizon Crossings</b>	<b>36</b>

<b>7 Orbital Velocity</b>	<b>37</b>
<b>8 Atmospheric Cross Section</b>	<b>39</b>
<b>9 Effective Transmittance Model</b>	<b>41</b>
<b>10 Importance of Argon</b>	<b>43</b>
<b>11 Importance of Longitude and Latitude</b>	<b>45</b>
<b>12 Concluding Remarks about Preliminary Simulations</b>	<b>48</b>
<b>Part III: Conclusions</b>	<b>50</b>
<b>13 Final Words and Future Directions</b>	<b>50</b>
13.1 Improvements to HCNMl . . . . .	51
13.1.1 Use of X-ray Data Below 1 keV . . . . .	52
13.2 Use of the C Statistic . . . . .	53
<b>14 References</b>	<b>54</b>
<b>A Additional HCNM Results</b>	<b>57</b>
<b>B Inputs to the NRLMSISE-00 Density Model</b>	<b>57</b>
<b>C Additional Information</b>	<b>58</b>
<b>D Additional Figures</b>	<b>59</b>
<b>E Table of Symbols</b>	<b>61</b>

## List of Figures

1.1	February 3, 2020 Horizon Crossing as observed by the NICER X-ray telescope on the ISS. During the horizon crossing, NICER follows V4641 Sgr as it comes out from behind the rocky surface of Earth and radiation penetrates Earth's atmosphere. The y-axis plots photon arrival counts binned at one second intervals and the x-axis is the time since the start of NICER's observation of V4641 Sgr. . . . .	2
1.2	NICER-detected horizon crossing of the Crab Nebula. . . . .	3
1.3	Horizon Crossing of Sco X-1 detected by the Ginga satellite in 1989 . . . . .	6
1.4	Ginga Remake plots . . . . .	6
1.5	Values of $\delta t_{hc}$ plotted against $N_0$ from both NICER horizon crossings. The standard error $\delta t_{hc}$ is defined by the $\chi^2 + 1$ test, which is described in Section 5.3.3. The temporal errors $\delta t_{hc}$ should be multiplied by orbital velocity ( $\sim 7.6$ km/s) to get in-track positional errors, $\delta r_{hc}$ . This figure is re-printed from Ruhl et al. (2022). . . . .	8
3.1	Simplified diagram of a horizon crossing where the source direction, $\hat{\mathbf{s}}$ , is projected into the vector $\hat{\mathbf{s}}_{\text{proj}}$ that lies in the plane of the orbit. The orbital plane is defined by the pole unit vector $\hat{\mathbf{h}}$ . In this diagram, the inner circle is a planet and the outer circle is the satellite's path. The satellite moves counter clockwise through the horizon crossing, starting with a line of sight that is tangent to the planet's surface at $\mathbf{r}_0$ , and ending with a line of sight that is tangent to the orbital path at $r_2$ . The symbols $s_0$ , $s_3$ , and $s_\infty$ indicate points on the line of sight. . . . .	13
3.2	This diagram shows the right triangle used in the derivation of Equation (6), which gives the position of $\mathbf{r}_{0,2d}$ . The value of $\mathbf{r}_{0,2d}$ provides an initial estimate of the satellite's position at the start of the crossing, $\mathbf{r}_{0,3d} = \mathbf{r}_{0,hc}$ . . . . .	14
3.3	Algorithm to locate $\mathbf{r}_{0,2d}$ in a circular orbit model. The argument of perigee, $\omega_p$ is set to zero for the circular orbit. . . . .	14
3.4	3D model of a horizon crossing. This diagram shows the point in time where a telescope's line of sight is tangent to the Earth's surface (it <i>grazes</i> the Earth). In this diagram, we can see that even if two satellites perform the same exact orbit, they observe the start of a horizon crossing at a different position and time ( $\mathbf{r}_0$ and $t_0$ ), which depends on how far away the source is from the orbital plane. . . . .	15
3.5	Diagram of the perifocal ( $\{\hat{\mathbf{p}}, \hat{\mathbf{q}}, \hat{\mathbf{w}}\}$ ) and geocentric-equatorial ( $\{\hat{\mathbf{I}}, \hat{\mathbf{J}}, \hat{\mathbf{K}}\}$ ) coordinate frames. This diagram is re-printed from the textbook "Orbital Mechanics for Engineering Students" by Howard D. Curtis (Curtis, 2005). The $\{\hat{\mathbf{I}}, \hat{\mathbf{J}}, \hat{\mathbf{K}}\}$ frame is described by $\{\hat{\mathbf{x}}, \hat{\mathbf{y}}, \hat{\mathbf{z}}\}$ in this paper. . . . .	16
5.1	Geodetic vs "geocentric" altitude. Geocentric altitude is the supplementary angle to the polar angle, $\phi$ used in Equation (20). This image is reprinted from the Penn State University online class notes here: <a href="https://www.e-education.psu.edu/geog862/book/export/html/1669">https://www.e-education.psu.edu/geog862/book/export/html/1669</a> . . . . .	21

5.2	Convolutions of source count rate from NICER can be used to estimate orbital period of the ISS. . . . .	22
5.3	Spectrum of V4641 Sgr smoothed and then normalized so that the area under the 1.0 - 2.1 keV range is equal to unity. This spectrum can operate as a probability distribution of detected photon energies when we consider NICER data between 1.0 keV and 2.1 keV. . . . .	24
5.4	X-ray transmittance of 1.0 - 2.1 keV photons during a horizon crossing. The orange curve represents the X-ray transmittance that we expect will go through Earth's atmosphere and get detected by NICER. The blue dots represent the transmittance as collected by NICER, $T = N/N_0$ . The origin of the plot, although set to zero on the x-axis labels, represents $t_{0,e}$ , and the x-axis shows the elapsed time after $t_{0,e}$ during the horizon crossing. . . . .	25
5.5	Visualization of the “ $\chi^2 + 1$ test” used to estimate HCNM measurement uncertainty. This plot corresponds to the 1.0 – 2.0 keV energy band in the V4641 Sgr. horizon crossing. . . . .	26
5.6	This diagram shows the symbols and methods used to analyze the error of HCNM. We predict the satellite to be located at $\mathbf{r}_{0,\text{hc}}$ at the time $t_{0,e}$ , but if $t_{0,e} \neq t_{0,mkf}$ , the predicted satellite orbit contains an extra source of in-track error, $\Delta r_e$ . We introduce the position $\mathbf{r}_{0,e}$ which can be compared to $\mathbf{r}_{0,mkf}$ directly, since they both occur at the time $t_{0,mkf}$ . $R_{\text{orbit}}$ is the estimated orbital radius in our model, while $R_{\text{orbit},mkf}$ represents the instantaneous radius of the ISS orbit. . . . .	29
5.7	BCMC fits of photo-electric cross section plotted against the piecewise $\sigma(E) \propto E^{-3}$ function, which is fit to the XCOM data points in green. The BCMC cross sections are much more accurate than the piecewise model, as they are fit to more data and use a more complicated functional form. . . . .	32
7.1	Tangent altitude increases more rapidly with time when the ISS moves at a faster orbital velocity. . . . .	37
7.2	Transmittance curves when altering orbital velocity for the 2.0 – 3.0 keV energy band. The transmittance models correspond to the circular orbit model on the day of the V4641 Sgr. horizon crossing. . . . .	38
7.3	In-track error as a function of error in orbital velocity for different X-ray energy bands. . . . .	39
8.1	Curves of transmittance vs tangent altitude slide to the left or right on the time axis when cross section is altered and the same density model is used. . . . .	40
8.2	In-track error versus scaling factor, $\alpha$ , of the atmospheric cross section. . . . .	40
8.3	Photo-electric cross section as a function of Energy. Cross sections retrieved from Balucinska-Church and McCammon (1992). . . . .	41

9.1	Transmittance model curve compared to binned photon events from the Crab Nebula horizon crossing. This plot shows that an “effective transmittance” model with steps of $dx=0.25$ keV within the $1.0 - 2.0$ keV energy band is needed in order to best fit the shape of the data. . . . .	42
9.2	Effective transmittance model curves for $2.0 - 3.0$ keV photons compared to data from the Crab Nebula. The plot shows that $dx=0.5$ keV is needed to best fit the shape of the data. . . . .	43
10.1	Plot of elemental photo-electric cross sections as a function of photon energy (Balucinska-Church and McCammon, 1992). . . . .	44
11.1	Mass Density in Earth’s atmosphere, plotted as relative difference from equatorial density. . . . .	46
11.2	Difference between the MSIS-00 longitudinally-averaged density profile and the density profile defined at the grazing point. . . . .	47
13.1	Expected transmittance curve vs transmittance data as detected by NICER for the $0.3 - 1.0$ keV energy band. . . . .	52
13.2	Photoelectric cross sections of Earth’s major atmospheric constituent (Balucinska-Church and McCammon, 1992) . . . . .	53
2.1	Latitude and longitude of tangent point during the crossing of V4641 Sgr. Since the latitude and longitude of the tangent point do not change much throughout the horizon crossing, we use a single density profile as a function of altitude calculated at the grazing point (gp). . . . .	58
4.1	Comparison of the exact density profile and the longitudinally-averaged density profiles used in Section 11. . . . .	59
4.2	Summary of the four main steps involved in an HCNM measurement. This diagram starts by assuming that the input orbital model is already defined, but it can also be defined from the “cool start” formulation described in Part II. . . . .	60

## List of Tables

5.1	Values of $t_{0,mkf}$ , $\mathbf{r}_{0,mkf}$ , and $\mathbf{r}_{0,he}$ calculated using the oblate earth model. Uncertainties in each vector component correspond to the (0.01 second) time steps of our numerical model orbit: $x \pm 0.01$ km, $y \pm 0.03$ km, $z \pm 0.03$ km. $n = 0.1$ km steps were used when simulating the line of sight. . . . .	28
5.2	Calculated values of $t_{0,e}$ for six partially overlapping energy bands when using the model of Earth as an ellipsoid. For reference, $t_{0,mkf} = 367.25$ sec (Table 5.1). . .	28

5.3	Error analysis of the V4641 Sgr. horizon crossing using a circular model orbit, a model of Earth as an ellipsoid, and the model of $\sigma(E)$ given in Equation 19. The symbol $\Delta r_{tot}$ represents the total error in locating $\mathbf{r}_{0,mkf}$ , and $\Delta r_e$ represents the part of the total error due to the horizon crossing measurement. The unattenuated count rate represents the average number of counts per 1 second bin at the top of a transmittance curve. . . . .	31
5.4	Values of $t_{0,mkf}$ , $\mathbf{r}_{0,mkf}$ , and $\mathbf{r}_{0,hc}$ calculated for a spherical earth. Uncertainties in each vector component corresponding to the (0.01 second) time steps of our numerical model orbit are $x \pm 0.01$ , $y \pm 0.03$ , and $z \pm 0.03$ . . . . .	33
5.5	Error analysis of the V4641 Sgr. horizon crossing using a circular model orbit, a model of Earth as a sphere, and the model of $\sigma(E)$ given in Equation 19. $\Delta r_{tot}$ represents the total error in locating $\mathbf{r}_{0,mkf}$ (the “best estimate” of position if it is only known that Earth is a sphere), and $\Delta r_e$ represents the part of the total error due to the atmospheric model. $\Delta r_e$ is a result of $\Delta t_e$ . . . . .	34
5.6	Weighted means of the results of the V4641 Sgr. horizon crossing in the cold start scenario. This table shows the weighted means of the results of Tables 5.3 and 5.5. . . . .	35
9.1	Drop in atmospheric cross section within individual energy bands from 1.0 – 5.0 keV. The values in this table are determined from Table 8.3. . . . .	42
10.1	Results of the V4641 Sgr. horizon crossing when using an atmospheric cross section consisting of 78% N and 22% O. The “mkf” positions and BCMC cross sections are used in the calculations of these results. . . . .	44
10.2	Results of the Crab Nebula horizon crossing when using an atmospheric cross section consisting of 78% N and 22% O. The “mkf” positions and BCMC cross sections are used in the calculations of these results. . . . .	45
11.1	Results of the V4641 Sgr horizon crossing using a density profile that is averaged over all longitudes . . . . .	47
11.2	Results for the Crab Nebula horizon crossing using a longitudinally-averaged density profile. . . . .	47
11.3	Weighted means of HCNM results when using a density profile averaged over all longitudes (Tables 11.1 and 11.2). . . . .	48
A.1	Results from the horizon crossing of V4641 Sgr using the “mkf” orbital solution as the input model, an ellipsoidal Earth, and BCMC cross sections. $\Delta t_{hc}$ is the error in correctly identifying $t_{0,mkf}$ , the time at which the spacecraft is at the position $\mathbf{r}_{0,mkf}$ . $\Delta r_{hc}$ is the in-track error corresponding to $\Delta t_{hc}$ . The uncertainties $\delta t_{hc}$ and $\delta r_{hc}$ are related to the number of attenuated counts in a given energy band. This table is re-printed from Ruhl et al. (2022). . . . .	57
A.2	Results from the horizon crossing of V4641 Sgr. using a circular orbit model, an ellipsoidal Earth, and BCMC cross sections. This table can directly be compared to Table A.1 in order to see the effect of an input orbit model that is not exact. . . . .	57

A.3	Results for the horizon crossing of the Crab Nebula when comparing only the portions of the data when NICER is confidently locked-on. The results are calculated using the “mkf” orbital solution as the input model, an ellipsoidal Earth, and BCMC cross sections. This table is re-printed from Ruhl et al. (2022). . . . .	57
B.1	Inputs to the MSISE-00 atmospheric model to extract profiles of density as a function of altitude. Longitude and Latitude correspond to the “graze point” (gp), the point on the telescopic line of sight where tangent altitude equals zero, which is shown in Figure 3.1. Geomagnetic Ap indices are provided by GFZ German Research Centre for GeosciencesMatzka et al. (2021). The f10.7 cm solar flux is provided by Space Weather Canada (1 sfu = $10^4$ Jy). . . . .	58
C.1	Right ascension, declination, and out-of orbital plane angle ( $\psi$ ) of the black hole binary V4641 Sgr and the Crab Nebula. The position of the ISS at the start of the horizon crossing, $\mathbf{r}_{0,mkf}$ , is given in terms of latitude, longitude, and altitude.	58
E.1	Table of symbols used in the Horizon Crossing Navigational Method (HCNM) . .	61

# 1 Introduction

## 1.1 Current Methods of Deep Space Navigation

Navigating a spacecraft far from Earth is one of the greatest challenges of modern space exploration because the methods that we use rely heavily on relaying radio signals back-and-forth between Earth and the spacecraft. For this reason (in addition to multiple others), our possibilities for deep space navigation are severely limited by a destination's distance from Earth. Since we rely on communication with radio waves that travel at the speed of light, it can take a very long time to determine the location of a spacecraft or probe on a deep space mission. Just to go to Neptune and back to Earth takes light almost 17 hours. This is one of the many reasons why it is highly desirable to create methods of autonomous navigation that run on-board a spacecraft without any human intervention. Extracting navigational information from the stars, a technique that has been used by sailors for centuries, is likely to be our best chance at achieving autonomous navigation and exploring new worlds. As we will see in this paper, X-ray wavelengths and X-ray stars have qualities that can be exploited in order to perform autonomous navigation.

The current best option for deep space navigation is The Deep Space Network (DSN), which is an international network of radio antennas spaced out at  $120^\circ$  on Earth in a way that allows constant observation of space as Earth rotates (Emadzadeh and Speyer, 2011). In order to determine the position of spacecraft, DSN uses a combination of Earth-based radar ranging and on-vehicle optical imaging, a method in which a camera on the spacecraft takes pictures of the surrounding space, planets, asteroids, and stars (Emadzadeh and Speyer, 2011). By the nature of radar ranging, the error in radial position determination is proportional to the spacecraft distance from Earth and its performance is significantly limited in the two transverse directions (Ray et al., 2008). Optical tracking, on the other hand, has the potential to be very accurate for navigation near planets, but it requires very complex and expensive cameras and image-processing software (Emadzadeh and Speyer, 2011). It is estimated that the DSN can achieve position accuracies on the order of 1-10 km per AU of distance from Earth (Emadzadeh and Speyer, 2011). Moreover, the DSN is expensive to maintain and is always busy supporting concurrent mission (Emadzadeh and Speyer, 2011). For these reasons, autonomous celestial-based navigation is highly desirable and can revolutionize possibilities for space exploration. X-ray navigation provides an opportunity to determine high precision navigational information from X-ray data collected from sensors on-board the spacecraft, without any communication with Earth.

## 1.2 Introduction to Horizon Crossings

A horizon crossing is the event in which a celestial source, emerging from behind the rocky surface of a planet, comes into the line of sight of a telescope that is on a satellite. If the planet has an atmosphere, the telescope observing the horizon crossing will detect the onset of photons at different times based on their energies. Specifically, the telescope will detect higher energy photons earlier in time than lower energy photons, since higher energy photons are more likely

to penetrate the denser, lower sections of the atmosphere (Figure 3.1). As demonstrated by Ruhl et al. (2022), knowing the atmospheric model of a planet enables one to predict the transmittance of X-ray photons during a horizon crossing. Comparing the expected transmittance model to binned X-ray data can provide high precision information about the orbital position of the satellite in both space and time.

Horizon crossings require purposeful programming of the telescope so that it will look through a planet’s atmosphere even before it detects radiation from the source. The Neutron Star Interior Composition Explorer (NICER) X-ray telescope on the International Space Station (ISS) successfully viewed its first horizon crossing on February 3, 2020. During this crossing, NICER observed the black hole binary V4641 Sagittarii (V4641 Sgr), a relatively faint black hole binary and X-ray source with a brightness of about 600 counts per second as collected by NICER. NICER also observed a second horizon crossing on August 11, 2022, a crossing of the Crab Nebula. The horizon crossing of the Crab Nebula, a source that is  $\sim 20\%$  times brighter than V4641 Sgr, is shown in Figure 1.2. The stratification of energy bands present in Figures 1.1 and 1.2 would not appear in a plot of count rate versus time for a normal “attitude acquisition”, in which the telescope does not track the source through the planet’s atmosphere. A horizon crossing around a planet with no atmosphere, such as the Moon, would look like a Heaviside step function.

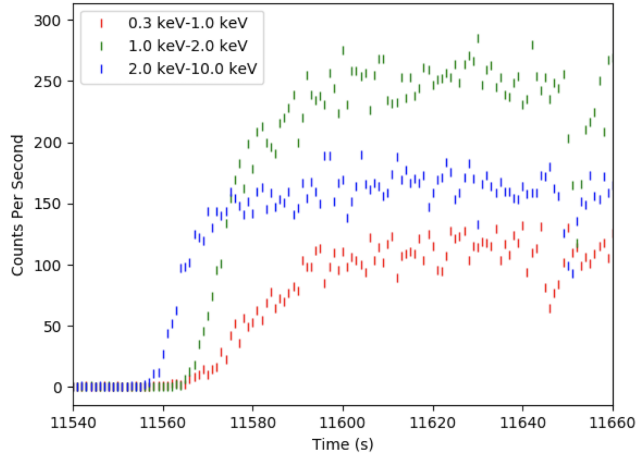


**Figure 1.1** February 3, 2020 Horizon Crossing as observed by the NICER X-ray telescope on the ISS. During the horizon crossing, NICER follows V4641 Sgr as it comes out from behind the rocky surface of Earth and radiation penetrates Earth’s atmosphere. The y-axis plots photon arrival counts binned at one second intervals and the x-axis is the time since the start of NICER’s observation of V4641 Sgr.

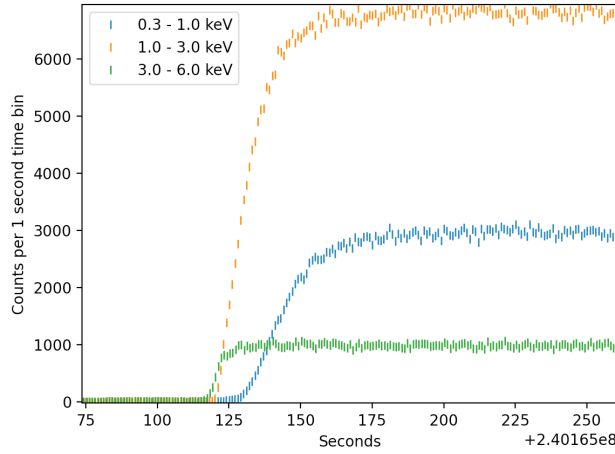


**Figure 1.2** NICER-detected horizon crossing of the Crab Nebula.

Horizon crossings are of great interest because they present a variety of applications. Not only can horizon crossings be used for on-board, autonomous navigation, but they can also be used for atmospheric science. Horizon crossings are very similar to the technique of “X-ray Occultation Sounding” (XOS), which Determan et al. (2007) used to measure atmospheric density. An occultation is essentially the opposite of a horizon crossing, since the satellite moves further away from the source, descending in its orbit and looking through a column of atmosphere that becomes more and more dense (the satellite motion is the opposite of that shown in Figure 3.1). In this way, the curve of count rate versus time starts at the source’s full, unattenuated count rate (in a given energy range) and decreases to zero, instead of starting at zero and increasing to the unattenuated count rate (as shown in Figures 1.1 and 1.2). In our analysis of the horizon crossing, we adapt concepts and remote sensing techniques that Determan et al. (2007) used to analyze occultations, specifically the concept of the “tangent point altitude” (shown in Figure 3.1) and Beer’s law (Equation 17), as well as the motivation behind analyzing X-ray absorption in a planetary atmosphere.

There are two ways to study horizon crossings: one where you use knowledge of the location of a satellite/telescope to improve your atmospheric model (Roble and Hays (1972), Determan et al. (2007), and Katsuda et al. (2021)), and the other where you use knowledge of a planet’s atmosphere to find the location of the telescope. In this paper, we present a “proof of concept” for the latter navigational problem, and develop the Horizon Crossing Navigational Method (HCNM). We propose a method that uses an atmospheric model of Earth in order to precisely predict where and when photons of certain energies will be detected by NICER during the orbit of the ISS. X-ray navigational methods, such as HCNM, will become particularly relevant as humans explore new and potentially habitable planets where it is not possible to use many existing navigational techniques, such as satellite GPS or ground station tracking.

The navigational precision of horizon crossings requires an in-depth analysis of cost and benefit where you must consider how well you know the atmosphere, the size, and the shape of the orbited planet (we will analyze how much the shape of the Earth affects the accuracy of HCNM in Section 5.5) and also how well you can model the satellite’s orbit before conducting the horizon crossing (Wood, 1993). For example, in the case where the satellite’s position is well-defined (e.g. defined by GPS or previous applications of HCNM), the error in predicting the transmittance curve, or equivalently the *measurement error*, can be on the order of 0.01 seconds, but if there is significant uncertainty in the cross-track position, radial position, or velocity of the initial orbit estimate during the horizon crossing, the error may be above 0.1 seconds. Multiply these time errors by the linear velocity of the satellite, let’s say  $v = 7 \text{ km/sec}$  for LEO, and you get the corresponding in-track position error, 7 meters and 700 meters respectfully. By conducting multiple horizon crossings one after another, orbital trajectory can continually be updated and improved (for example, Lambert’s problem in orbital mechanics can be used to describe an orbit from an input of two position vectors at two times), so even if the first horizon crossing results in a 700 meter in-track residual in the “cool start” scenario that is developed in this paper, a 7 meter in-track accuracy can be obtained after subsequent horizon crossings. The method of analysis presented in Section 5.5 also provides the first steps necessary to quantitatively understand the uncertainty in a HCNM-estimated position given an inputted orbital model, which is crucial to any feedback-control system.

As Wood and Ray (2017) explain in their historical review of the NRL program in X-ray Navigation, XNAV is the most general term for X-ray navigation. NRL focused their navigation program on analyzing two features of the X-ray sky: (1) persistent variability of sources, such as pulsations and (2) transitions of stars with known positions, such as occultations, eclipses, and horizon crossings (Wood and Ray, 2017). In this way, XNAV and HCNM exploit the two major features of the X-ray sky and fall under the umbrella term of XNAV. The two areas of focus for NRL utilize the fact that features of the X-ray sky that are precise and predictable. While Millisecond Pulsars (MSPs) spin at a highly constant and predictable rate, bright X-ray point sources have a highly constant and predictable position in the sky. Since the brightest X-ray point sources are located at distances of  $1 - 10$  kiloparsecs ( $1 \text{ kiloparsec} = 3 \times 10^{21} \text{ cm}$ ), their proper motions on the sky are less than 10 milliarcseconds per year, and therefore it often takes a century for their apparent positions in the sky to change (Wood, 1993). For this reason, both MSPs and bright X-ray stars can operate as “navigational beacons” in two different ways.

In this paper, we will present the fundamental concepts of HCNM through the lens of a “cool start” problem: one where we determine the position of the satellite despite knowing ample information about it’s orbit. We will report results from analyzing NICER’s horizon crossing of V4641 Sgr on February 3, 2020, and we will consider the accuracy of HCNM in two different scenarios: one where we describe the Earth as an oblate spheroid and one where we describe the Earth as a perfect sphere. For each of these scenarios, we evaluate the accuracy of the navigational method in five photon energy bands from 1.0 - 5.0 keV. Comparing the results for the two different shapes of Earth is particularly important for HCNM, because when humans

visit a distant planet, we may not be able to determine its shape more accurately than a spherical approximation. Additionally, it is important to know the efficacy of HCNM in different energy bands, as there will be more opportunities to do horizon crossings on different celestial sources if the atmospheric model is accurate for a wide range of X-ray energies.

### 1.3 History of X-ray Navigation

X-ray navigation has a rich history that started at the Naval Research Laboratory (NRL) in the late 1980's, and the idea of X-ray navigation was ultimately made possible by the study of X-ray astronomy (Wood and Ray, 2017). Since Earth's atmosphere strongly absorbs X-rays at altitudes below 50 km, X-ray astronomy did not exist until the advent of sounding rockets after World War II, which carried X-ray sensors to high altitudes (Wood, 1993). By the 1990's, the X-ray sky had been surveyed several times and nearly  $10^5$  sources had been catalogued, many of which had precise features that the NRL planned to exploit for navigational purposes (Wood, 1993). The NRL-801 Experiment, also known as the Unconventional Stellar Aspect (USA) aboard the Air Force ARGOS (P91-1) satellite was launched in 1991 and was the first experiment (before NICER/SEXTANT in 2017) to systematically study the possibility of X-ray Navigation (Wood, 1993). The USA navigational experiments and the subsequent research focused mainly on attitude determination and celestial timekeeping with pulsars, and subsequent PhD theses by John Hanson and Suneel I. Sheikh (2005) were integral in further developing these methods of navigation (Wood and Ray, 2017). NRL researchers also identified the possibility of using horizon crossings for position determination (Wood, 1993), but many of these ideas were not further developed until Ruhl et al. (2022).

As noted by Wood and Ray (2017) and Wood et al. (2020), the first ever horizon crossing that was analyzed for navigational purposes was detected by the Japanese satellite Ginga in 1989. The observation of Scorpius X-1 (Sco X-1) crossing over the Earth's horizon, which is shown in Figure 1.3 was detected unintentionally. High solar activity caused Ginga to lose altitude so rapidly that the orbital solution, and thus the planned observation of Sco-X1, did not go as planned (Wood et al., 2020). In this way, Ginga happened to be pointing at Sco X-1 while the neutron star was still below Earth's horizon, and it stayed locked on Sco X-1 as it transitioned out of Earth's shadow. The natural logarithm of X-ray intensity versus time during the horizon crossing is shown in Figure 1.3. The various colors represent different X-ray energy bands. The highest energy X-rays appear first in time since they are able to penetrate Earth's atmosphere at lower altitudes than the lower energy photons, which start to appear when the line of sight of the X-ray detector goes through a less dense atmospheric column.

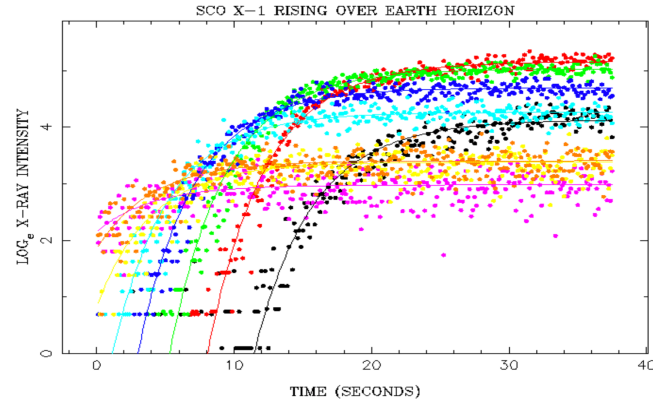


**Figure 1.3** Horizon Crossing of Sco X-1 detected by the Ginga satellite in 1989

As shown in Figure 1.3, NRL guest investigators fit transmittance curves to the crossing of Sco X-1. Wood and Ray (2017) claim that the time residuals of these fits correspond to 350 meters of in-track accuracy for the satellite in its orbit. Although the details of the Ginga horizon crossing are not available, our horizon crossing analysis produces results similar to the 350 meters of accuracy achieved in the Ginga horizon crossing. As shown by Ruhl et al. (2022), the horizon crossing of V4641 Sgr. provides an in-track position correction with an accuracy of 800 m, while the horizon crossing of the Crab Nebula, a source that is 20 times brighter, provides 170 m of in-track accuracy. It is important to note that the transmittance curves for the NICER horizon crossings shown in Figure 1.4 are not fit to the data at all, but rather they are predicted. Using a model of the Earth's atmosphere, we can predict the transmittance curve that the X-ray detector will see as it emerges from behind Earth's shadow, which is how we propose to use horizon crossings for navigation.

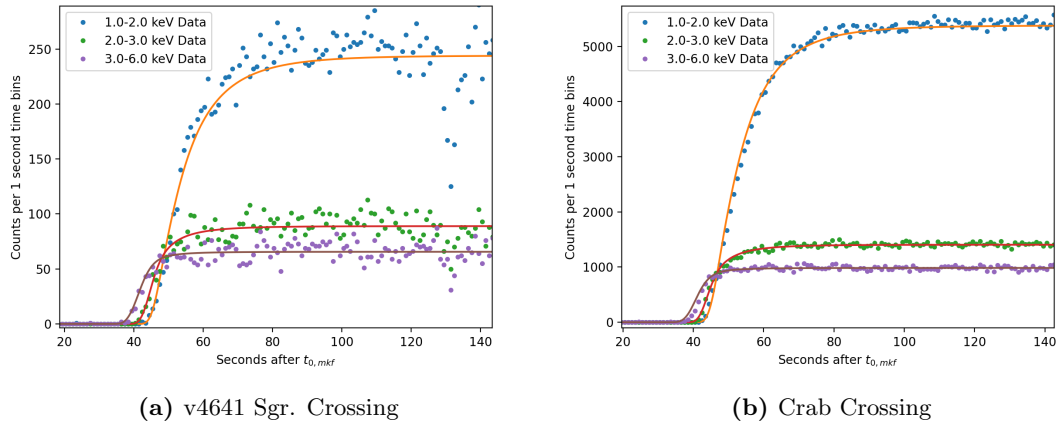


**Figure 1.4** Ginga Remake plots

## 1.4 The Vision of X-ray Navigation

The most well-developed method of X-ray navigation, which is known as XNAV, exploits the highly predictable nature of pulsars over long timescales, and provides a Global Positioning System (GPS)-like navigation (Sheikh et al., 2006; Winternitz et al., 2013). The first real-time, on-board, and autonomous demonstration of XNAV was performed aboard the ISS in 2017 and 2018 in a technology demonstration named SEXTANT, The Station Explorer for X-ray Timing and Navigation Technology (Mitchell et al., 2018). The main idea behind this technology is that MSPs rotate at a very constant rate (with millisecond periods), which enables them to act as extremely accurate clocks for navigation (Mitchell et al., 2018). In this method, the time at which a pulse is expected to arrive at the solar system barycenter (SSB) is compared with the time at which the pulse is detected by an X-ray detector aboard a spacecraft. By simultaneously comparing these times of arrivals (TOA's) for three or more pulsars, it is possible to determine the full three-dimensional position of the spacecraft with respect to the SSB. Moreover, ground-based and space-based telescopes continually update every pulsar's *ephemeris* and record its pulse period to high precision, which ensures the accuracy of MSPs for navigation even as their rotation slows down over long periods of time (Mitchell et al., 2018). In 2017, XNAV was able to maintain a less-than 10 km root-sum-squared (RSS) navigation error over a period of five days (Mitchell et al., 2018).

Wood et al. (2020) and Ruhl et al. (2022) propose that HCNM can be used in conjunction with the pulsar navigation method (XNAV) to perform more efficient navigation near and around planets. XNAV does not work well for spacecraft near or orbiting around planets, since the spacecraft is at risk of experiencing high accelerations in low-altitude orbit, thus affecting pulsar timing. Additionally, planetary occlusions significantly reduce the frequency of potential pulsar observations. In this way, XNAV is more suitable for interplanetary trajectories, while horizon crossings can be used near planets. One of the main advantages of using horizon crossings for navigation over pulsar navigation is that achievable position determination for XNAV is determined by the speed of light multiplied by the accuracy in measuring pulse TOA's,  $c\delta t_{toa}$ , while accuracy of position determination for horizon crossings is based on the accuracy in measuring the time of the horizon crossing multiplied by the spacecraft's velocity,  $v\delta t_{hc}$  (Wood et al., 2020). This gives horizon crossings an advantage of a factor of

$$F = \frac{c\delta t_{toa}}{v\delta t_{hc}}. \quad (1)$$

As shown by Ruhl et al. (2022),  $\delta t_{hc} = 30$  ms can be determined from a NICER-detected horizon crossing of the Crab Nebula, while  $\delta t_{toa} = 30\mu\text{s}$  is often achievable with the millisecond pulsars used by SEXTANT. For spacecraft in low-earth orbit, traveling at about 7 km/sec, horizon crossings can be 43 times as accurate as XNAV (Ruhl et al., 2022). Moreover, since horizon crossings can make use of the brightest stars in the X-ray sky, this advantage could potentially be much larger (Wood et al., 2020). On the other hand, the accuracy of XNAV does not have the same potential for growth, since candidates for pulsar navigation are limited to the most

predictable MSPs, which are inherently older and less bright than younger pulsars (Ray et al., 2008).

Figure 1.5 shows a plot of  $\delta t_{hc}$  vs  $N_0$ , the number of “unattenuated” counts detected in an energy band when the total source flux is not attenuated by the planet’s atmosphere. As we will see in Section 5.3.3, the value of  $\delta t_{hc}$  is used to estimate the accuracy of the horizon crossing measurement and is highly dependent on the brightness of the source. The data points for  $\delta t_{hc}$  in Figure 1.5 come from the results of the Crab Nebula and V4641 Sgr horizon crossings and show that  $\delta t_{hc} \propto 1/\sqrt{N_0}$ , where  $N_0$  is the number of unattenuated counts in a one second time bin. As we will discuss in Section 5.3.3, in general, the navigational accuracy attainable by an X-ray point source is inversely proportional to the square root of its intensity,  $I$ :

$$\delta t_{hc} \propto \frac{1}{\sqrt{I}}. \quad (2)$$

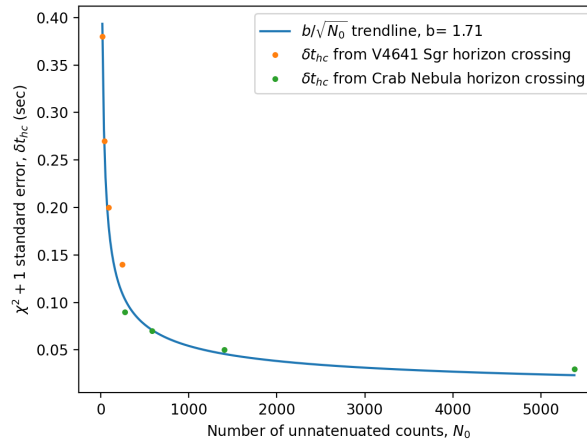


**Figure 1.5** Values of  $\delta t_{hc}$  plotted against  $N_0$  from both NICER horizon crossings. The standard error  $\delta t_{hc}$  is defined by the  $\chi^2 + 1$  test, which is described in Section 5.3.3. The temporal errors  $\delta t_{hc}$  should be multiplied by orbital velocity ( $\sim 7.6$  km/s) to get in-track positional errors,  $\delta r_{hc}$ . This figure is re-printed from Ruhl et al. (2022).

Since XNAV performs best in deep space, where measurement of pulse TOA’s is unaffected by orbital accelerations and planetary atmospheres, and since horizon crossings are only achievable near planets, the two methods of X-ray navigation are highly complementary (Wood et al., 2020). In practice, XNAV could be used for navigation in between planets and could provide HCNM with an initial orbital solution when the spacecraft arrives at the planet. Multiple sequential horizon crossings could then be performed in order to maintain and improve an orbital description individually, or the horizon crossings could provide an additional measurement for a joint Kalman filter with XNAV (Wood et al., 2020).

The methods could also be complimentary because XNAV requires an initial estimated state with accuracy of less than 0.5 km and less than 5 m/sec in order to achieve convergence of its navigational algorithm with RSS errors below 10 km (Mitchell et al., 2018); conducting 2 or more horizon crossings could provide XNAV with a reliable initial state estimate of position and velocity. After the XNAV solution converges, another horizon crossing could be conducted to predict an even more accurate position, or the spacecraft could leave orbit for deep space missions. Alternatively, horizon crossings could simply provide in-track information (as time or angular displacement from the last ascending node) into a Kalman Filter, or even as an input to improve GPS readings in Earth orbit.

Moreover, Wood et al. (2020) explain that horizon crossings can also be used for navigation around planets without atmospheres, and uses a Lunar occultation of the Crab Nebula detected by the Rossi X-ray Timing Explorer (RXTE) satellite in 2011 as an example. In this scenario, the *ingress* (nebula disappearing behind the moon) and *egress* (nebula re-appearing about 30 seconds later) are of particular importance for navigation, since the transition of the Crab pulsar into and out-of occultation can be timed and the relative phase of pulses detected just before ingress and directly after egress can be compared. The method described here vastly differs from HCNM because HCNM does not take advantage of Pulsar timing. In this way, X-ray transitions (horizon crossings, occultations, and eclipses) can be studied and performed in multiple different ways in order to obtain high-precision navigational information, however the joint horizon crossing/pulsar timing method has not yet been developed.

## 1.5 Dual Use of X-ray Horizon Crossings

In addition to using the same X-ray detector as XNAV, there is another major benefit of HCNM. Similar to optical navigation, HCNM can be used for the dual purpose of studying an unknown planetary atmosphere and for navigation. X-ray horizon crossings can be analyzed both to measure the atmosphere using a known satellite position, and to determine the satellite's position using a known atmosphere. Even if the navigational solution and the atmospheric solution start out with significant error after the first couple horizon crossings, while performing more horizon crossings, the two solutions would iteratively improve each other. This method of "dual use" has not yet been developed, but it would likely involve combining the methods of Roble and Hays (1972) and the methods presented in this paper. Combining the two problems would be a very important capability as we explore distant planets that have unknown atmospheres.

## 1.6 NICER Specifications

NICER's X-ray Timing Instrument (XTI) consists of a collection 56 aligned X-ray concentrator optics (XCO) and silicon drift detectors (SDD)(Gendreau et al., 2016). All together, NICER has an effective area of  $1900 \text{ cm}^2$  at 1.5 keV and an energy bandpass of 0.2 – 12.0 keV (Gendreau et al., 2016). The large effective area of NICER is ideal for detecting a large number of counts during a horizon crossing, but NICER is not necessarily the ideal instrument for detecting horizon

crossings. As discussed by Ruhl et al. (2022), NICER has difficulty pointing towards Earth’s limb, and thus has a hard time maintaining pointing control during a horizon crossing. During the horizon crossing of the Crab Nebula, NICER was late to “lock-on” to the Crab, which affected the results of HCNM and had to be considered in the data analysis (Ruhl et al., 2022). NICER is one example of an instrument that can perform both XNAV and HCNM, but future missions that carry X-ray-based avionics can be designed to more easily point towards a planet’s limb than NICER.

## Part I: HCNM and the “Cool Start” Scenario

### 2 Formulation of the Navigational Problem

The navigational problem that we solve in Part I of this paper is a variation of the cold start problem for a circular orbit, which we call a “cool start”. Although the low altitude orbit of the ISS is highly dynamic and is periodically boosted to maintain its orbital altitude in the LEO environment (Wood et al., 2020), we decided to model it as a circular orbit in order to demonstrate HCNM in simple terms. In this navigational problem, we assume that we know the shape of the planet around which we are orbiting (described as a sphere or as an ellipsoid), the mass of the planet, and the planet’s atmospheric model, which includes atmospheric density as a function of altitude above sea level and atmospheric absorption cross section as a function of energy (described in Section 4).

We assume that the satellite’s orbit is circular, that we know the position of the source ( $\hat{\mathbf{s}}$  is described by  $\hat{\mathbf{x}}$ ,  $\hat{\mathbf{y}}$ , and  $\hat{\mathbf{z}}$  in planet-centered inertial coordinates, or earth-centered inertial (ECI) in this paper), and that we know an accurate pole vector for the period of the orbit in which the horizon crossing occurs (we will use the unit vector  $\hat{\mathbf{h}}$ ). In terms of Keplerian Orbital elements, we know the eccentricity and the argument of perigee for a circular orbit ( $e = \omega_p = 0$ ), the inclination of the orbit ( $i$ ), and the right ascension of the ascending node ( $\Omega$ ). The line of nodes unit vector  $\hat{\mathbf{n}}$ , a unit vector that points in the direction of the orbit’s ascending node is given by Equation (3). The ascending node of an orbit is the point where a satellite crosses the (celestial) equatorial plane when traveling in the northerly direction.

$$\hat{\mathbf{n}} = \frac{\hat{\mathbf{z}} \times \hat{\mathbf{h}}}{|\hat{\mathbf{z}} \times \hat{\mathbf{h}}|}. \quad (3)$$

For a circular orbit, the Keplerian elements are given by the following formulas (Bate et al., 2020):

$$\begin{aligned} e &= \omega_p = 0 \\ i &= \cos^{-1}(\hat{h}_z) \\ \Omega &= \cos^{-1}(\hat{n}_x) \end{aligned} \quad (4)$$

where if  $\hat{n}_y > 0$ , then  $\Omega < 180^\circ$ . In summary, it is necessary to know the basic geometric description of the orbit, basic information about the planet, and a basic atmospheric model in order to locate the in-track position of the satellite. This formulation of HCNM is extremely unique and powerful because it enables us to connect the geometric description of the orbit with a temporal description, thus fully describing the satellite’s circular orbit. The first step to implement a temporal description is to calculate the orbital period (Section 5.3.1), and the next step is to use the horizon crossing to measure the time  $t_{0,e}$  at which the ISS is located at a position  $\mathbf{r}_{0,he}$  (the “e” subscript reminds us that  $t_{0,e}$  is calculated based on a specific energy

band, while  $\mathbf{r}_{0,hc}$  is a single value for a given orbital scenario and source location). If a satellite were to do multiple horizon crossings looking at different sources within a single orbit, we could find multiple pairs of  $\mathbf{r}_{0,hc}$  at  $t_{0,e}$ , and it would then be possible to track the orbit using standard techniques and perform differential adjustments to the orbital description.

### 3 Geometry of a Horizon Crossing

In order to analyze a horizon crossing, we first consider a simplified 2-dimensional scenario in which the unit direction vector to X-ray source,  $\hat{\mathbf{s}}$ , is projected into the (extended) plane of the orbit, so the unit vector pointing to the “projected” source position is  $\hat{\mathbf{s}}_{proj}$ . For this scenario, we will develop an analytical formula for  $\mathbf{r}_{0,2d}$ , the satellite’s position when the telescope’s line of sight is tangent to the planet’s surface. We will then consider the 3-dimensional scenario in order to define the better estimate  $\mathbf{r}_{0,3d}$ , which we will define as  $\mathbf{r}_{0,hc}$  moving forward. The position  $\mathbf{r}_{0,hc}$  represents the “start” of a horizon crossing for a given source position and orbital model. Unlike the 2-dimensional scenario, there is not a simple geometric formula for  $\mathbf{r}_{0,hc}$ , so we use an iterative numerical method, which is described in Sections 3.2.1 and 5.3.2.

After determining the position  $\mathbf{r}_{0,hc}$ , the next step in the analysis is to identify the time  $t_{0,e}$  at which the satellite is located at  $\mathbf{r}_{0,hc}$ . We will discuss this method in Section 5.3.3, as it is easier to understand with reference to the X-ray data.

#### 3.1 Two-Dimensional HC Geometry

##### 3.1.1 Position of Satellite at Crossing: a Two-Dimensional View

A two-dimensional model of a horizon crossing is shown in Figure 3.1 below, where we define the position of the start of the horizon crossing to be  $\mathbf{r}_{0,2d}$  ( $\mathbf{r}_0$  in the diagram). In Figure 3.1, the source is projected into the plane of the orbit, and the full line of sight to the source lies in the (extended) plane of the orbit. The unit vector pointing to the source,  $\hat{\mathbf{s}}$ , is projected into the plane of the orbit to create the unit vector  $\hat{\mathbf{s}}_{proj}$ , which is given by the following equation:

$$\hat{\mathbf{s}}_{proj} = \frac{\hat{\mathbf{s}} - (\hat{\mathbf{s}} \cdot \hat{\mathbf{h}}) \cdot \hat{\mathbf{h}}}{|\hat{\mathbf{s}} - (\hat{\mathbf{s}} \cdot \hat{\mathbf{h}}) \cdot \hat{\mathbf{h}}|}. \quad (5)$$

As indicated in Figure 3.1, since the X-ray source is so far away from Earth, the direction vector of the telescope’s (projected) line of sight does not change throughout the crossing and is equal to  $\hat{\mathbf{s}}_{proj}$ . Additionally, in order for  $\hat{\mathbf{s}}_{proj}$  to be constant,  $\hat{\mathbf{h}}$  must also be constant. The vector pole of the ISS orbit,  $\hat{\mathbf{h}}$ , precesses with a 60 day period, so on the  $\sim$ 300 second timescale of a horizon crossing (or even the timescale of multiple orbits),  $\hat{\mathbf{h}}$  is approximately constant.

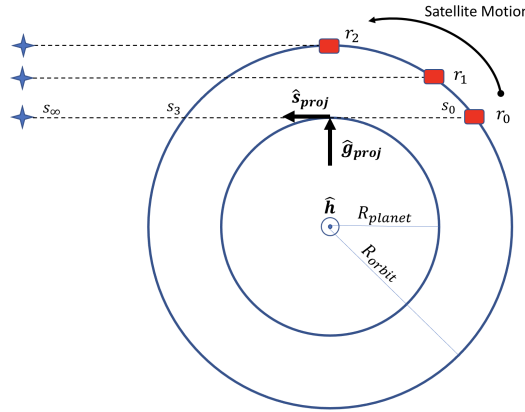


**Figure 3.1** Simplified diagram of a horizon crossing where the source direction,  $\hat{s}$ , is projected into the vector  $\hat{s}_{proj}$  that lies in the plane of the orbit. The orbital plane is defined by the pole unit vector  $\hat{h}$ . In this diagram, the inner circle is a planet and the outer circle is the satellite's path. The satellite moves counter clockwise through the horizon crossing, starting with a line of sight that is tangent to the planet's surface at  $\mathbf{r}_0$ , and ending with a line of sight that is tangent to the orbital path at  $r_2$ . The symbols  $s_0$ ,  $s_3$ , and  $s_\infty$  indicate points on the line of sight.

Although this figure simplifies the geometry of a real horizon crossing by projecting the position of the source into the orbital plane, it still provides intuition about where the horizon crossing occurs in space. The formulas defined below can help us estimate the location (in planet-centered inertial coordinates)  $\mathbf{r}_0$  on the satellite's orbital path. As shown in Figure 3.1, the position  $\mathbf{r}_0$  is the satellite position for which the telescopic line of sight is tangent to the planet's surface. Figure 3.1 also shows that  $\hat{g}_{proj}$ , a (projected) unit vector that points to the location where the telescopic line of sight *grazes* the planet's surface, can be defined as  $\hat{g}_{proj} = \hat{s}_{proj} \times \hat{h}$ . As shown in Figure 3.2, the triangle with hypotenuse  $A = \sqrt{R_{orbit}^2 - R_{earth}^2}$  can help us translate from  $\hat{g}_{proj}$  to  $\mathbf{r}_{0,2d}$ . In this way, we can define  $\mathbf{r}_{0,2d}$ , which operates as an initial estimate for  $\mathbf{r}_{0,HC}$ .

$$\mathbf{r}_{0,2d} = R_{earth} \cdot \hat{g}_{proj} - A \cdot \hat{s}_{proj}. \quad (6)$$

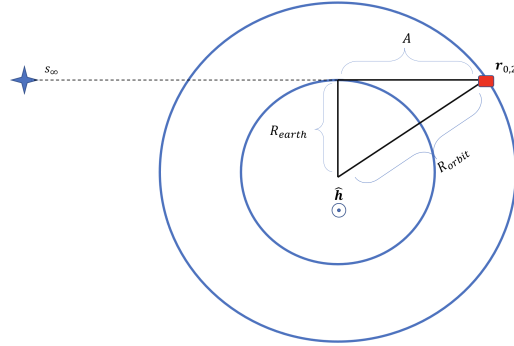


**Figure 3.2** This diagram shows the right triangle used in the derivation of Equation (6), which gives the position of  $\mathbf{r}_{0,2d}$ . The value of  $\mathbf{r}_{0,2d}$  provides an initial estimate of the satellite's position at the start of the crossing,  $\mathbf{r}_{0,3d} = \mathbf{r}_{0,hc}$ .

Figure 3.3 shows one way to visualize the algorithm for locating  $\mathbf{r}_{0,2d}$  in a given orbit model. This plot shows our circular model orbit for the ISS orbit in the same orbital period as the horizon crossing. Time since the last ascending node is plotted on the x-axis and the black dashed line labeled “Intersection” marks the approximate time of the horizon crossing. As can be seen in Figure 3.3, the horizon crossing occurs at  $\sim 60\%$  in orbital phase from the ascending node, or equivalently at a “true anomaly” of  $\sim 220^\circ$ .

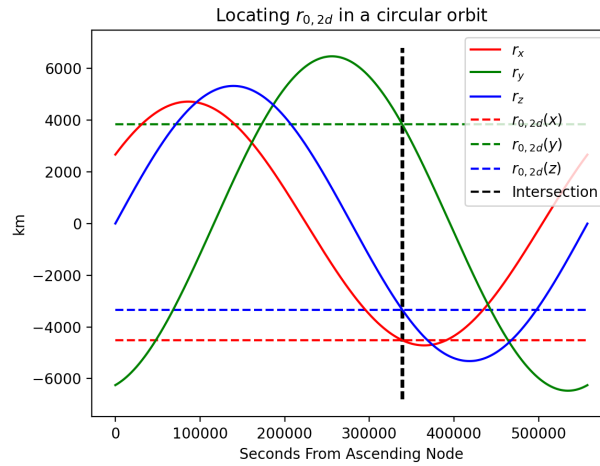


**Figure 3.3** Algorithm to locate  $\mathbf{r}_{0,2d}$  in a circular orbit model. The argument of perigee,  $\omega_p$  is set to zero for the circular orbit.

### 3.2 Three-Dimensional Geometry

Now, we have a value for  $\mathbf{r}_{0,2d}$ , but we must also account for the situation in which the source is an angle  $\psi$  out of the orbital plane (shown in Figure 3.4). In Section 3.2.1, we will show the formulas that describe  $\mathbf{r}_{0,hc}$ , and later in Section 5.3.2, we will explain the numerical algorithm that is used to solve these equations for  $\mathbf{r}_{0,hc}$ .

Figure 3.4 below shows a simplified model of two satellites (orange and green dots) performing the same orbit, but looking in different directions. The orange dot is looking at a “3D” source that is  $\psi = 22^\circ$  out of the plane of the orbit, and the other is looking at the same source, but it is projected into the orbital plane.

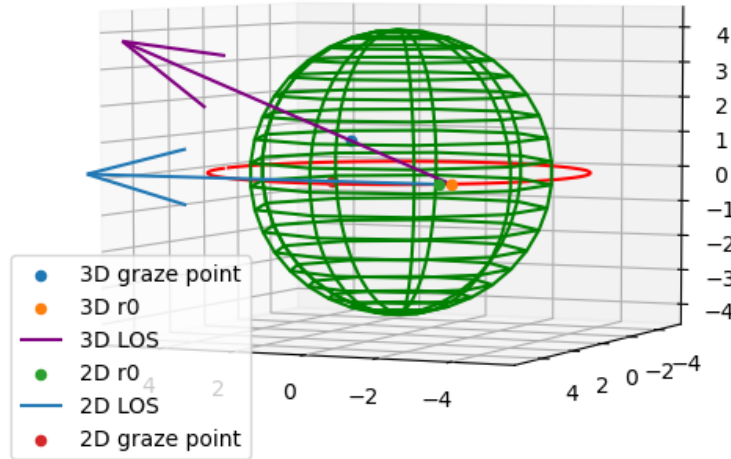


**Figure 3.4** 3D model of a horizon crossing. This diagram shows the point in time where a telescope’s line of sight is tangent to the Earth’s surface (it *grazes* the Earth). In this diagram, we can see that even if two satellites perform the same exact orbit, they observe the start of a horizon crossing at a different position and time ( $\mathbf{r}_0$  and  $t_0$ ), which depends on how far away the source is from the orbital plane.

In this diagram, the pole vector is pointing straight downwards, so the satellite is orbiting clockwise as viewed from above. The figure shows that the position vectors  $\mathbf{r}_{0,2d}$  and  $\mathbf{r}_{0,3d}$  ( $\mathbf{r}_{0,hc}$  is used in the text), the positions when the telescopes’ lines of sights are tangent to earth’s surface, are not the same. Since the orange dot is located to the right of the green dot on the orbital path,

we can determine that  $t_{0,3d}$  occurs earlier than  $t_{0,2d}$  from a geometric perspective. This shows the importance of developing a generalizeable method for any source that is an angle  $\psi$  out of the orbital plane. For a source with position  $\hat{\mathbf{s}}$ , the out-of-plane angle,  $\psi$ , is given in Equation (7) below. Additionally, it is important to remember that there is an upper limit to  $\psi$  for which a horizon crossing cannot occur, which is either determined by the orbital geometry (the ratio of planet radius to orbital radius) or the range of motion of the telescope's pointing range of motion. Specifically, because of NICER's limited field of regard on the ISS Express Palate, it can only observe horizon crossings of sources that are a couple degrees out of the orbital plane, whereas other detector systems that do not have this issue may be able to look up to  $\sim 20^\circ$  or  $30^\circ$  out-of-plane, depending on their orbit (Ruhl et al., 2022; Wood et al., 2020).

$$\psi = \frac{\pi}{2} - \cos^{-1}(\hat{\mathbf{h}} \cdot \hat{\mathbf{s}}) \quad (7)$$

### 3.2.1 Position of Satellite at Crossing: a Three-Dimensional View

In order to predict the position  $\mathbf{r}_{0,hc}$  of the satellite for which the telescope's line of sight (pointing towards  $\hat{\mathbf{s}}$ ) is tangent to Earth's surface, we first have to create an array of positions within our model of the perfectly circular ISS orbit. In order to describe the orbit, we use the *perifocal* reference frame, which sits on the plane of the orbit and is described by the unit vectors  $\hat{\mathbf{p}}$ ,  $\hat{\mathbf{q}}$ , and  $\hat{\mathbf{w}}$  in Figure 3.5.

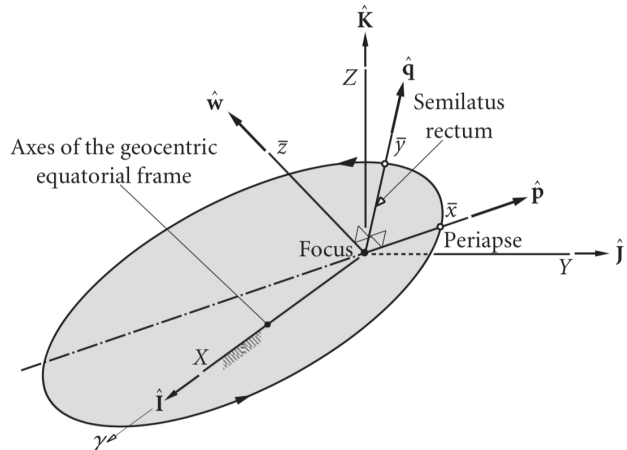


**Figure 3.5** Diagram of the perifocal ( $\{\hat{\mathbf{p}}, \hat{\mathbf{q}}, \hat{\mathbf{w}}\}$ ) and geocentric-equatorial ( $\{\hat{\mathbf{i}}, \hat{\mathbf{j}}, \hat{\mathbf{k}}\}$ ) coordinate frames. This diagram is re-printed from the textbook “Orbital Mechanics for Engineering Students” by Howard D. Curtis (Curtis, 2005). The  $\{\hat{\mathbf{i}}, \hat{\mathbf{j}}, \hat{\mathbf{k}}\}$  frame is described by  $\{\hat{\mathbf{x}}, \hat{\mathbf{y}}, \hat{\mathbf{z}}\}$  in this paper.

The position of a satellite in a circular orbit at any time  $t > t_0$  is described by the equation

$$\mathbf{r}_{per} = R_{orbit} \cdot [\cos(\omega(t - t_0))\hat{\mathbf{p}} + \sin(\omega(t - t_0))\hat{\mathbf{q}} + 0\hat{\mathbf{w}}], \quad (8)$$

where  $\omega = 2\pi/T$  is the angular velocity of the satellite's orbit. The  $[\mathbf{Q}]$  matrix in Equation (9) can be used to transform vectors between the perifocal and planet-centered coordinate frames (Curtis, 2005):

$$[\mathbf{Q}] = \begin{bmatrix} \cos(\Omega) \cos(\omega_p) - \sin(\Omega) \sin(\omega_p) \cos(i) & \sin(\Omega) \cos(\omega_p) + \cos(\Omega) \cos(i) \sin(\omega_p) & \sin(i) \sin(\omega_p) \\ -\cos(\Omega) \sin(\omega_p) - \sin(\Omega) \cos(i) \cos(\omega_p) & -\sin(\Omega) \sin(\omega_p) + \cos(\Omega) \cos(i) \cos(\omega_p) & \sin(i) \cos(\omega_p) \\ \sin(\Omega) \sin(i) & -\cos(\Omega) \sin(i) & \cos(i) \end{bmatrix} \quad (9)$$

so that

$$\mathbf{r}_{per} = [\mathbf{Q}]\mathbf{r}_{eci} \quad (10)$$

$$\mathbf{r}_{eci} = [\mathbf{Q}]^T \mathbf{r}_{per}. \quad (11)$$

After converting  $\mathbf{r}_{per}$  to  $\mathbf{r}_{eci}$ , we identify an array of positions in the orbit located near the point  $\mathbf{r}_{0,2d}$ . To be safe, we search within  $\pm 1.5\%$ , or equivalently  $\sim \pm 50$  km for the ISS orbit, of each vector component, although this range could be specified as a function of the out-of-plane angle  $\psi$  in order to better optimize software run time. Each of the position vectors in this array is a possible  $\mathbf{r}_{0,hc}$ , and we identify the correct  $\mathbf{r}_{0,hc}$  by enforcing that the telescopic line of sight corresponding to  $\mathbf{r}_{0,hc}$  is tangent to the planet's surface. The line of sight from the satellite towards the source,  $\mathbf{rs}$  is described by the following parametric equation:

$$\mathbf{rs} = \mathbf{r}_{0,hc} + n \cdot \hat{\mathbf{s}}. \quad (12)$$

As discussed in Section 1.6, X-ray sources are so far away that their positions stay relatively constant over the span of 100 years. Additionally, a source's far distance from Earth implies that its position relative to the satellite position is equal to its position relative to the planet-centered inertial coordinate system. Therefore, both direction vectors are equal to  $\hat{\mathbf{s}}$ , and for the case of a horizon crossing around Earth,  $\hat{\mathbf{s}}$  is determined by converting the source's position in terms of right ascension and declination into ECI coordinates through the following transformation  $((\alpha, \delta) \rightarrow (x, y, z))$ :

$$\begin{aligned} x &= \cos \delta \cos \alpha \\ y &= \cos \delta \sin \alpha \\ z &= \sin \delta. \end{aligned} \quad (13)$$

Moreover, the tangent and *grazing* line of sight has the property that only one point on the line of sight, as an example when  $n = k$ , is at a distance from the planet-centered origin equal to the radius of the orbited planet. Written as an equation, the correct  $\mathbf{r}_{0,\text{hc}}$  can be identified because it is the only position (in the range near  $\mathbf{r}_{0,\text{2d}}$ ) for which the following equation is true for a single, positive integer,  $k$ :

$$|\mathbf{rs}(k)| = |\mathbf{r}_{0,\text{hc}} + k \cdot \hat{\mathbf{s}}| = R_{\text{planet}}. \quad (14)$$

## 4 Atmospheric Model

The atmospheric model of the planet around which you are orbiting must include knowledge of the relative abundances, also known as *mixing ratios*  $C_g$ , of the  $g$  atmospheric constituents, the cross sections of total attenuation of each atmospheric constituent as a function of energy  $\sigma_g(E)$ , and the atmospheric density profile,  $\rho(z)$ , as a function of altitude from sea level to the altitude of the orbit. Alternatively, if density is not known but atmospheric temperature is known, density as a function of altitude can be solved from considerations of hydro-static equilibrium.

In order to analyze a horizon crossing, we must be able to predict the transmittance of X-ray photons that make it through a planet's atmosphere at different altitudes above the planet's surface. We define the transmittance  $T$ , which is given in Equation (15) as the detected photon count rate,  $N$ , divided by the source's total *unattenuated* count rate,  $N_0$ , both in a given energy band. A source's *unattenuated* count rate,  $N_0$ , is the count rate detected by a detector when there is no atmosphere to absorb or scatter photons.

$$T = \frac{N}{N_0}. \quad (15)$$

The cross sections  $\sigma_g(E)$  are “specific” cross sections in units of area divided by mass, and are known as *coefficients of total mass attenuation* because they include both attenuation due to scattering and absorption, since we only care about what photons get detected by a telescope, not the specific mechanism involved in the photon attenuation (Wood et al., 2002). However, since the photoelectric effect is almost entirely responsible for X-ray attenuation in the atmosphere, the “coefficient of total mass attenuation” is approximately equal to the “photoelectric absorption cross section” (Wood et al., 2002). For this reason, in Part II of this paper, we make use of the convenient and highly accurate photoelectric cross section fits created by Balucinska-Church and McCammon (1992). In Part I, we assume the general relationship for photo-electric cross section,  $\sigma \propto E^{-3}$ . Throughout the rest of the paper, we refer to  $\sigma$  as the “absorption cross section” or simply “cross section”. Equation (16) below gives the formula for the total cross section,  $\sigma(E)$ , of an atmosphere consisting of  $g$  constituent molecules.

$$\sigma(E) = \sum_g C_g \sigma_g(E) \quad (16)$$

In our definition of this total effective cross section, we use the average volumetric mixing ratio of Earth’s atmosphere below 85 km, 78% N<sub>2</sub>, 21% O<sub>2</sub>, 1% Ar, and assume that this stays constant above 85 km. Although the ratios do change slightly above 85 km, a simple mix like this works well for navigational purposes (Ruhl et al., 2022). In order to easily use Equation (16) in computations, we fit a piecewise function around the k-edge of Argon, using the general relationship  $\sigma \propto E^{-3}$ , which is valid for most atoms in the energy range where the photo-electric effect is the dominant attenuation mechanism. A molecule’s “k-edge” is defined as the energy required to emit a K-shell electron, which are the innermost and most tightly bound electrons. A key signature of the k-edge for a particular element is a discontinuous jump in absorption cross section, or equivalently, a sharp drop in transmittance when the photon energy is just above the k-edge (moving from right to left on a plot of  $\sigma$  versus energy).

Since extinction of soft X-rays is entirely due to photoelectric absorption, radiative transfer in an atmosphere can simply be described by Beer’s Law (Equation (17)), which is used to compute the transmittance,  $T$ , of X-ray photons through a column of atmosphere (Wood et al., 2002):

$$T = e^{-\tau}. \quad (17)$$

The value of  $\tau$ , the non-dimensional optical depth, is determined by integrating the product of atmospheric density and absorption cross section along the telescopic line of sight, and represents a measure of atmospheric transparency (Determan et al., 2007). The exact optical depth for the line of sight of a telescope in orbit to a source (a limb-looking geometry) is given by the indefinite integral in Equation (18):

$$\tau = \int_{s_0}^{s_\infty} \sigma(E) \rho(z) ds \quad (18)$$

where  $ds$  is an infinitesimal step along the line of sight and  $z$  is the radial altitude from earth’s surface to a point on the line of sight. We use units for  $\sigma(E)$ ,  $\rho(z)$ , and  $ds$  to ensure that  $\tau$  is dimensionless: cm<sup>2</sup>/g, g/cm<sup>3</sup>, and cm. When computing this integral numerically, we take the upper bound to be the value of  $s$  corresponding to the radial altitude above Earth’s surface of the satellite’s orbit.  $s_0$  and  $s_\infty$  for a single line of sight are defined in Figure 3.1. In Section 5.3, we will discuss how to use Beer’s Law to predict the transmittance curve of a specific source as it comes into view of a telescope.

## 5 Application to the ISS orbit

### 5.1 Atmospheric Model of Earth

In our model of Earth’s atmosphere, we use values of density as a function of altitude from the Naval Research Laboratory’s MSISE-00 model (Picone et al., 2002). The MSIS model accepts inputs of date and time, latitude and longitude, as well as the solar flux “f10.7” cm solar flux index and the geomagnetic “ap” index. Tables B.1 of Appendix B show the parameters used when extracting density profiles from the MSIS-00 model for the two horizon crossing observations.

In Part I and certain parts of Part II of this paper, we use values of absorption cross section from the XCOM database managed by the National Institute of Standards and Technology (NIST) (Berger and Hubbell, 1987). We inputted earth's average atmospheric mix (78% N<sub>2</sub>, 21% O<sub>2</sub>, 1% Ar) into the XCOM database, and Equation (16) was used to produce a table of the net cross section data from 1.0 keV to 5.0 keV. Accounting for the k-edge of oxygen at 3.2 keV, we fit the cross section data to the following piecewise equation where  $E$  is in keV and  $\sigma$  is in  $\text{cm}^2/\text{g}$ :

$$\sigma(E) = \begin{cases} 3537.12E^{-3} + 4666.35 & 1.0 \leq E < 3.203 \text{ keV} \\ 60.77E^{-3} + 1.24 & 3.203 \leq E \leq 5.0 \text{ keV} \end{cases} \quad (19)$$

In Part II, we will use functional fits to atomic photo-electric absorption cross sections created by Balucinska-Church and McCammon (1992), as was used by Ruhl et al. (2022). In this demonstration of the “cold start” problem in Part I, we use the NIST data and the simple piecewise function of  $\sigma(E)$  in order to demonstrate that both the total absorption cross sections and the photo-electric absorption cross sections are very similar for soft X-rays, and in Part II, we will consider how the different models affect the results of HCNM.

## 5.2 Oblate Model of Earth

From the perspective of satellites, even satellites in LEO such as the ISS at  $\sim$ 420 km, the Earth's shape is noticeably different from a sphere Wood and Ray (2017). It is particularly important for the horizon crossing method to consider the shape of the Earth as an oblate spheroid, since we rely on numerically “walking” along the telescopic line of sight to find when it is tangent to Earth's surface.

In order to model the Earth as an ellipsoid, we use the 1984 model from the World Geodetic System (Macomber, 1984). The semi-major axes (equatorial radii) are  $a = b = 6378.137$  km and the semi-minor axis is  $c = 6356.7523$  km. The parametric equation of this ellipsoid is described by Equation (20), where  $\theta$  is the azimuthal angle and  $\phi$  is the polar angle.

$$\begin{aligned} x &= a \cos(\theta) \sin(\phi) \\ y &= b \sin(\theta) \sin(\phi) \\ z &= c \cos(\phi) \end{aligned} \quad (20)$$

Because of the symmetry of the reference ellipsoid about the z-axis, only the polar angle  $\phi$  needs to be specified when determining the altitude of a specific point above the Earth's surface. In this way, Equation 20 can be used to determine the distance of any point on a telescopic line of sight from the origin of the ECI coordinate system, or a “geocentric” altitude. In the study of geodesy, there is a slightly more precise value called the “geodetic” altitude, which ensures that the altitude of a point is measured perpendicular to Earth's surface. However, the difference between geocentric altitude and geodetic altitude is only  $\sim$ 70 m at 45° latitude on Earth's surface and at altitudes into the atmosphere, and thus does not affect the calculation of transmittance

curves very much (Clynnch, 2006). Since the transmission of soft X-rays occurs at altitudes above 80 km, atmospheric density is decreasing at a much smaller rate than near sea level and therefore this  $\sim 70$  m difference is not very significant. Figure 5.1 shows a diagram of the difference between geocentric and geodetic latitude, and the altitude is shown by the continuation of the dotted lines above Earth's surface. We have compared the performance of HCNM with geocentric and geodetic altitudes, and have seen that the geocentric approximation is always consistent with results when using geodetic altitudes within the level of precision specified by  $\delta t_{hc}$ . Calculating the geocentric altitude is also slightly more computationally efficient than calculating the geodetic altitudes. For these reasons, it is accurate to use polar angles and geocentric altitudes at this point in the development of HCNM, especially for the “cool start” problem.

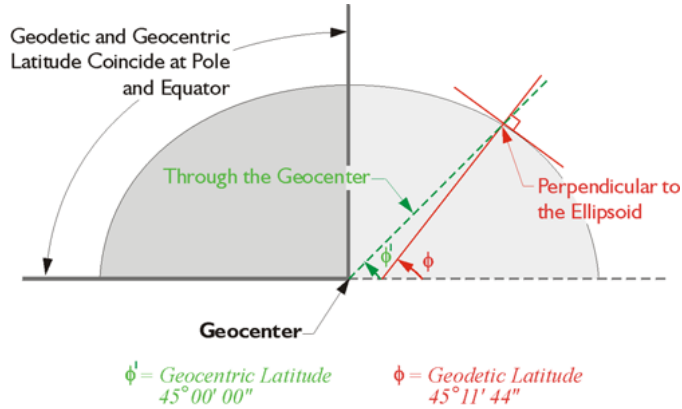
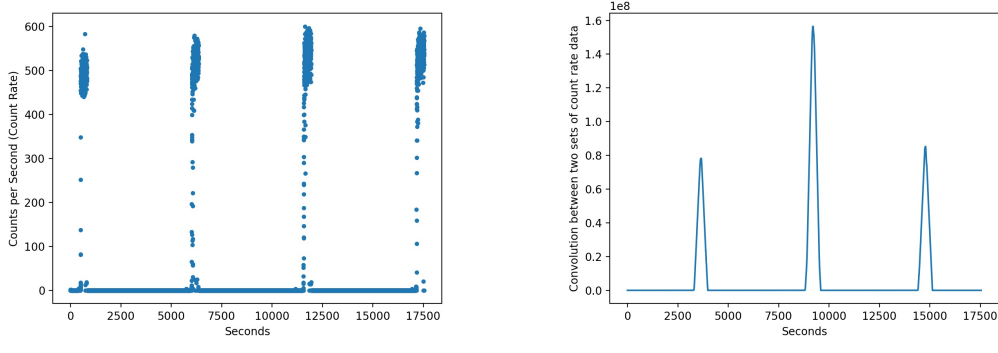


**Figure 5.1** Geodetic vs “geocentric” altitude. Geocentric altitude is the supplementary angle to the polar angle,  $\phi$  used in Equation (20). This image is reprinted from the Penn State University online class notes here: <https://www.e-education.psu.edu/geog862/book/export/html/1669>

## 5.3 The Navigational Method

### 5.3.1 Calculating Orbital Period

As explained in Section 2, we treat the pole of the orbit as the only known variable that describes the satellite’s orbit. The next step to further describing the satellite’s orbit is to introduce a temporal description, and we will consider one possible method of introducing a temporal description that agrees with our formulation of a cool start navigational problem: one that only uses NICER-collected X-ray counts. We perform a convolution on the count rate data, splitting Figure 5.2a in two halves and convolving them together (alternatively, one could find the principle frequency of the Fourier series). Figure 5.2a shows the count rate data from NICER during the three orbits surrounding the horizon crossing and Figure 5.2b shows a plot of the convolution.



(a) Counts per second detected by NICER when observing V4641 Sgr. on February 3, 2020 for three full orbits.

(b) Convolution of count rate data in Figure 5.2a. The average time between the three spikes is the first estimate of orbital period.

**Figure 5.2** Convolutions of source count rate from NICER can be used to estimate orbital period of the ISS.

The average time between peaks in Figure 5.2b is an estimate of the orbital period:  $T_{guess} = 5566.5$  seconds. However, since the ISS orbit is much more complicated than a perfect circle, we improved the value of  $T_{guess}$  by considering a subsequent observation of V4641 Sgr on January 31, 2021. We calculated the total  $\Delta t = 72.8$  hours between peaks in the convolutions from February 3 and the observation on January 31, and then divided  $\Delta t$  by the initial  $T_{guess}$ , and we calculated 47.08 orbits between the peaks of the two convolutions. Since there could only have been an integer number of orbits between those two points (neglecting effects of precession), we calculated a better estimate for orbital period,  $T_{best} = T_{guess}/47 = 5576.7$  seconds. Based on the radius of the orbit during the horizon crossing and Kepler's Third Law (Equation (21)), the best estimate for an orbital period is 5577.8 seconds.

We calculated the angular velocity of the orbit to be  $\omega = 2\pi/T_{best} = 1.267 \cdot 10^{-3}$  rad/sec, and the orbital radius to be  $R_{orbit} = 6796.4$  km. Using the value of  $T_{best}$ ,  $R_{orbit}$  was calculated using Kepler's Third Law:

$$R_{orbit}^3 = \frac{T_{best}^2 GM_{earth}}{4\pi^2}. \quad (21)$$

### 5.3.2 Locating the Position of the ISS at Crossing

Using the method described in Section 3.2.1, we identified the array of position vectors  $\mathbf{r}_{0,model}(t)$  that are close to  $\mathbf{r}_{0,2d}$  ( $\pm 1.5\%$  of each vector component, which is a safe range for this orbital geometry). The method to locate the three-dimensional position of the ISS at the start of the horizon crossing,  $\mathbf{r}_{0,hc}$ , requires checking what vector within  $\mathbf{r}_{0,model}(t)$  satisfies Equation (14). For every position vector within  $\mathbf{r}_{0,model}(t)$ , we consider the line of sight corresponding to the satellite's position at the corresponding time,  $t$ . The line of sight at the time  $t$  is defined by the

following parametric equation:

$$\mathbf{rs}(t) = \mathbf{r}_{0,\text{model}}(t) + n \cdot \hat{\mathbf{s}}. \quad (22)$$

Note that Equation (22) is the equation of the real “3D” line of sight, since it uses  $\hat{\mathbf{s}}$  of V4641 Sgr, which is  $2.58^\circ$  out of the plane of the ISS orbit. We will see the consequences of modelling the ISS orbit as a perfect circle in  $\mathbf{r}_{0,\text{model}}(t)$  in Section 5.5.

We then numerically walk along the line of sight at every  $t$  and check to see if any point on the line of sight “grazes” Earth’s surface, which occurs when the point on the line of sight with the smallest magnitude from the (geocentric) origin is greater than the radius of Earth (Equation (14)). To be safe, we let  $n$  span between 0 km and  $2A \approx 4735$  km, although the distance to the graze point will be a couple hundred kilometers larger than  $A$  depending on the out-of-plane angle of the source. Making use of vectorization in Python (with Numpy) or any other language that supports vectorization, it is not computationally expensive to check a large range of  $n$  values for the point on the line of sight that grazes Earth’s surface. If the grazing point does not occur in the range of  $n$  values, we move forward in time to the next satellite position  $\mathbf{r}_{0,\text{model}}(t + \Delta t)$  and check for grazing again, which occurs when the satellite is at the position  $\mathbf{r}_{0,\text{hc}}$ . For example, using the line-of-sight defined at  $\mathbf{r}_{0,\text{hc}}$ , we found that the grazing point on the line of sight occurs at a distance  $n_{\text{graze}} = k = 2375.5$  km from the ISS for the oblate Earth model and a distance of  $k = 2368.0$  km for the spherical Earth model. Using the results of this algorithm, the vector to the three-dimensional graze point can be defined as  $\mathbf{g} = \mathbf{r}_0 + k \cdot \hat{\mathbf{s}}$ .

When considering the Earth as an ellipsoid, this procedure is slightly more complicated, as the magnitude of each point along the line of sight must be compared to the planet-centered radius corresponding to that specific point on the line of sight. Every point along the line of sight  $\mathbf{rs}(n)$  will have a “polar angle” that is defined by

$$\phi(n) = \frac{\mathbf{rs}(n)_z}{|\mathbf{rs}(n)|} \quad (23)$$

where  $\mathbf{rs}(n)_z$  is the  $z$  component of the position vector to a point  $n$  km along the line of sight. The polar angle is the complement of the geocentric latitude as shown in Figure 5.1. We then plugged in  $\phi(n)$  into the parametric equation of the ellipsoid in Equation (20), and subsequently calculated the altitude above Earth corresponding to the specific point along the line of sight. As discussed above, because of the symmetry of Earth, the azimuthal angle does not affect the magnitude of the vector  $\mathbf{rs}(n)$ , so the radius of the planet is the same for any azimuthal angle. We arbitrarily set  $\phi = 0$ .

### 5.3.3 Identifying the Time of Crossing

In order to locate  $t_{0,e}$ , the start of the horizon crossing as determined by a given energy band of X-rays, we use Beer’s Law (Equation 17) to predict the transmittance curve that would be detected by the telescope during the crossing. Locating  $t_{0,e}$  is a multi-step process, and the first step is to collect the source’s spectrum in order to calculate a transmittance model that is specific

for the source of interest – in this case, V4641 Sgr. Since we use a spectrum collected by NICER, it is not necessary to consider the detector’s response matrix. Additionally, the gold on NICER’s X-ray detector has an absorption edge at 2.2 keV, which appears in NICER-collected spectra. In order to reduce the effects of the gold edge and other variability, we used a Fourier Transform to smooth out the higher frequency components of spectrum.

We then normalize the source’s spectrum such that the area under a chosen energy range is equal to unity, which is shown for the 1.0 - 2.1 keV energy band in Figure 5.3 below. In this way, the normalized spectrum can operate as a probability distribution of photons emitted by the source within the 1.0 - 2.1 keV energy range.

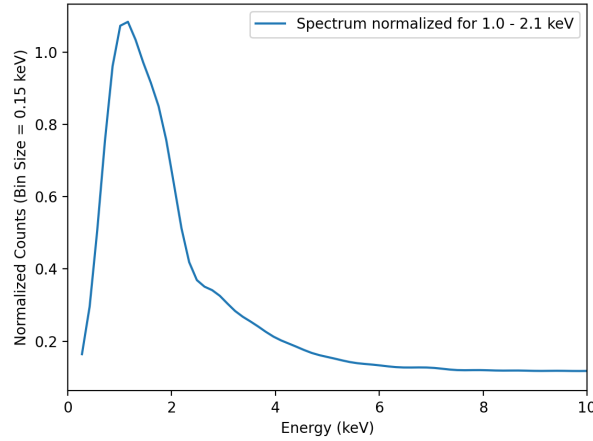


**Figure 5.3** Spectrum of V4641 Sgr smoothed and then normalized so that the area under the 1.0 - 2.1 keV range is equal to unity. This spectrum can operate as a probability distribution of detected photon energies when we consider NICER data between 1.0 keV and 2.1 keV.

Using the spectrum as a probability distribution, we calculate a curve for the total “effective” transmittance curve for the 1.0 – 2.0 keV band,

$$T_{eff} = \sum_i P_i T_i \quad (24)$$

where the  $i$  index steps through the 1.0 - 2.1 keV energy range,  $P_i$  is the area under the normalized spectrum and  $T_i$  is the transmittance calculated from Beer’s Law. In Section 9, we will discuss the importance of the effective transmittance model. The transmittance  $T_{eff} = T(E, t)$  is a function of X-ray and energy and time  $t$  after  $t_0$ , which is given by

$$T(E, t) = e^{-\tau(E, t)} \quad (25)$$

$$\tau(E, t) = \int_{s_0}^{s_3} \sigma(E) \rho(z) ds, \quad (26)$$

where we have replaced the  $s_\infty$  of the indefinite integral (Equation 17) with  $s_3$  (defined in Figure 3.1). In order to perform the numerical integration across the line of sight, we use a variation of the equation of the line of sight defined in Equation (22), and in this case, we replace  $\mathbf{r}_{0,\text{model}}$  with  $\mathbf{r}_{\text{model}}$ , which is a model of the satellite's circular orbit for the  $\sim 300$  seconds following  $\mathbf{r}_{0,\text{hc}}$ . We therefore define the line of sight at time any time  $t \geq t_0$  with the following equation:

$$\mathbf{r}_{\text{S}}(t) = \mathbf{r}_{\text{model}}(t) + n \cdot \hat{\mathbf{s}} \quad (27)$$

We then use Equation (27) in conjunction with our atmospheric model in order to evaluate the optical depth in Equation (26) and compute effective transmittance for the 1.0 - 2.1 keV energy band. As shown in Figure 5.4 below, we were able to predict both the shape and the location in time of the X-ray transmittance curve to a high degree of accuracy for the 1.0 - 2.1 keV energy band. Using the MSIS model for atmospheric density (Picone et al., 2002) and the effective transmittance model, we predict the shape and location of the transmittance curves well for all energy bands from 1.0 - 5.0 keV. As we will see in Section 5.5, the accuracy in locating  $t_{0,e}$  is also highly dependent on  $\sigma(E)$ . An error in  $\sigma(E)$  would lead to an incorrect prediction of the transmittance curve on the time axis.

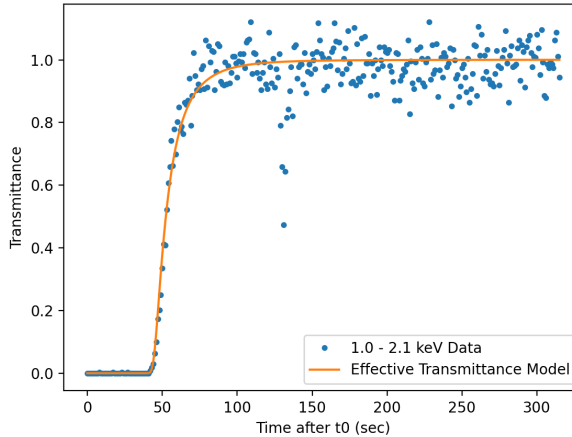


**Figure 5.4** X-ray transmittance of 1.0 - 2.1 keV photons during a horizon crossing. The orange curve represents the X-ray transmittance that we expect will go through Earth's atmosphere and get detected by NICER. The blue dots represent the transmittance as collected by NICER,  $T = N/N_0$ . The origin of the plot, although set to zero on the x-axis labels, represents  $t_{0,e}$ , and the x-axis shows the elapsed time after  $t_{0,e}$  during the horizon crossing.

We then scale the model and data transmittance curves by the source's unattenuated count rate in the energy band,  $N_0$ , and slide the curve along the time axis across the NICER data points in order to find the location of the curves with the minimum value of chi squared. The equation of  $\chi^2$  used to align the model with the data is given in Equation (28), where we calculate  $\chi^2$  in

the range of 1% to 99% transmittance:

$$\chi^2 = \sum_k \frac{(O_k - E_k)^2}{E_k} \quad (28)$$

where  $O_k$  is the number of observed counts in the  $k$ 'th time bin and  $E_k$  is the number of expected counts. It is important to note that the denominator of  $\chi^2$  is defined as  $E_k$ , since the error associated with each bin of a counting experiment is  $\sqrt{E_k}$ . The value of  $t_{0,e}$  was then determined by reading the time corresponding to the origin of Figure 5.4. In order to estimate the uncertainty associated with aligning the two curves, we quote the uncertainty in  $t_{0,e}$  to be the amount of time required for  $\chi^2$  to increase by one on either side of the minimum value of  $\chi^2$ . Figure 5.5 shows the value of  $\chi^2$  when “sliding” a transmittance model past the X-ray data, and comparing the model to the X-ray data between 1% and 99% transmission. The red dotted lines indicate where the value of  $\chi^2$  increases by one on either side of the minimum, which represents the best alignment of the model and the data.

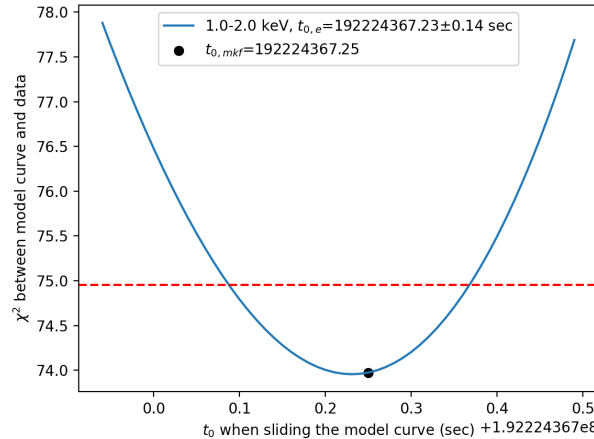


**Figure 5.5** Visualization of the “ $\chi^2 + 1$  test” used to estimate HCNM measurement uncertainty. This plot corresponds to the 1.0 – 2.0 keV energy band in the V4641 Sgr. horizon crossing.

It is also important to remark that the minimum of the curve in Figure 5.5 is at a value of  $\chi^2 \sim 74$ , while there are 58 data points used in the comparison. 58 data points are used in the comparison since the time range from 1% to 99% transmission contains 58 one-second time bins. These results lead to a reduced  $\chi^2$  of  $\sim 1.28$  at the best fit, which is a statistically sound comparison. Additionally, the  $\chi^2 + 1$  method correctly accounts for the uncertainty related to the Poisson statistics of binning photon events. As shown in Figure 1.5 of Section 1.6, the uncertainty is proportional to  $1/\sqrt{N_0}$  where  $N_0$  is the number of counts in a one second time bin. The  $\chi^2 + 1$  uncertainty shown in Figure 5.5 is equal to  $\delta t_{hc} = 0.14$  s, and is plotted as the third orange data point in Figure 1.5, where the source’s untenant count rate in the energy band is

250 counts. If bin sizes of 0.5 or 0.25 seconds are used in the analysis,  $N_0$  reduces to 125 and 62.5 counts per bin respectively, but  $\delta t_{hc}$  stays approximately constant. This finding is generally true of binned events and suggests that  $\delta t_{hc}$  is related to a source's intensity (as shown in Equation 2), rather than  $N_0$ , which depends on bin size. While sub-second binning increases the number of data points in the curve comparison time range, it also decreases the signal-to-noise ratio of the data. Additionally, sub-second binning significantly increases the run-time of HCNM analysis, and since we have not observed any particular performance benefit, we stay with one second time bins in this paper.

## 5.4 Reference Position of the ISS at Crossing

The diagram in Figure 4.2 of Appendix D summarizes the process of the HCNM measurement in four steps, the first three of which have been discussed in Sections 5.3.2 and 5.3.3, and the last of which will be described in Section 5.5.4. In order to determine the validity of our claim that the ISS is located at  $r_{0,hc}$  at the time  $t_{0,e}$ , we need to determine a best estimate of the *start of crossing*, which we denote as  $t_{0,mkf}$  and  $\mathbf{r}_{0,mkf}$  because we use NICER's ".mkf" file that contains the location of the ISS from NICER's GPS receiver.

Our method to solve for  $\mathbf{r}_{0,mkf}$  is similar to how we solved for  $\mathbf{r}_{0,hc}$  in Section 3.2.1: it uses the same exact technique of finding the location and time of the ISS when its line of sight is tangent to the Earth's surface. However, the method to calculate  $\mathbf{r}_{0,mkf}$  is more exact because instead of using a model ISS orbit that is propagated as a circle, we iterate through the actual positions of the ISS from the mkf-extension data file when we define the line of sight. Moreover, this method also enables the location of  $t_{0,mkf}$  which is a time from January 1, 2014, whereas the numerical method to locate  $\mathbf{r}_{0,hc}$  was strictly geometrical and did not provide any useful information about time (although time since the last ascending node could be determined, but we have yet to use that information in HCNM).

## 5.5 Results and Error Analysis

### 5.5.1 Note on Error Analysis

In Sections 5.3.2, we calculated a value  $\mathbf{r}_{0,hc}$ , which is a single, well-defined position vector for a specific  $\hat{\mathbf{h}}$  and  $\hat{\mathbf{s}}$ . Then in Section 5.3.3, we calculated values of  $t_{0,e}$ , which are specific to the energy band that we consider in a horizon crossing. Our final solution for the position of the ISS is then  $\mathbf{r}_{0,hc}$  at the time  $t_{0,e}$ . If  $t_{0,e} \neq t_{0,mkf}$ , this means that the atmosphere localizes the horizon crossing at an incorrect angular distance from the position in the satellite's orbit when the telescopic line of sight grazes Earth's surface. Because of this complication, in order to compare the results of HCNM to  $\mathbf{r}_{0,mkf}$  at  $t_{0,mkf}$ , we must introduce the position vector  $\mathbf{r}_{0,e}$ , which represents our estimated position of the ISS at the time  $t_{0,mkf}$ .

### 5.5.2 Oblate Earth Model

Using the numerical methods described in Sections 5.4 and 3.2.1 with 0.01 second time steps, we calculated the values of  $t_{0,mkf}$  and  $\mathbf{r}_{0,mkf}$  using the model of Earth as an ellipsoid, which are shown in Table 5.1 below. For ease of reading, all values of  $t_{0,mkf}$  and  $t_{0,e}$ , which are originally calculated as a number of seconds from January 1, 2014, are reported as a number of seconds after  $t = 192224000.00$  seconds.

Oblate Earth Model	
$t_{0,mkf}$	367.25 sec
$\mathbf{r}_{0,mkf}$ (km)	[-4512.40, 3844.34, -3326.14]
$\mathbf{r}_{0,hc}$ (km)	[-4512.24, 3843.04, -3326.82]

**Table 5.1** Values of  $t_{0,mkf}$ ,  $\mathbf{r}_{0,mkf}$ , and  $\mathbf{r}_{0,hc}$  calculated using the oblate earth model. Uncertainties in each vector component correspond to the (0.01 second) time steps of our numerical model orbit:  $x \pm 0.01$  km,  $y \pm 0.03$  km,  $z \pm 0.03$  km.  $n = 0.1$  km steps were used when simulating the line of sight.

The value of  $\mathbf{r}_{0,mkf}$  in Table 5.1 are regarded as the “exact” values of the ISS position and will be compared to the values of  $\mathbf{r}_{0,hc}$  and  $t_{0,e}$  resulting from the Horizon Crossing Method. In Section 5.5.3. The results of the algorithm to locate  $t_{0,e}$  (as described in Section 5.3.3) are shown in Table 5.2 below.

Oblate Earth Model				
Photon Energy Band	1.0 – 2.0 keV	2.0 – 3.0 keV	3.0 – 4.0 keV	4.0 – 5.0 keV
$t_{0,e}$	367.37 sec	366.82 sec	366.81 sec	367.09 sec

**Table 5.2** Calculated values of  $t_{0,e}$  for six partially overlapping energy bands when using the model of Earth as an ellipsoid. For reference,  $t_{0,mkf} = 367.25$  sec (Table 5.1).

As shown in Table 5.2, certain energy bands predict values of  $t_{0,e}$  that are closer to  $t_{0,mkf} = 367.25$  than other energy bands (Table 5.1). In this way, the atmospheric model used in this paper works best for certain energy bands. Our method to estimate the uncertainty in each of the measured values of  $t_{0,e}$  was introduced in Section 5.3.3 and will be used when analyzing the results. Figure 5.4 (Section 5.3.3) shows the precision with which our model predicts the transmittance curve for the 1.0 - 2.1 keV energy band.

The location of the transmittance curve on the time axis is most strongly related to the determination of  $t_{0,e}$ , but the comparison can also be altered by incorrectly predicting the shape of the curve. Based on observations and inspection of Beer’s Law (Equation 17), the shift of the curve on the time axis is most strongly dependent on the model of  $\sigma(E)$ , while the shape of the curve is more closely related to the density profile,  $\rho(z)$  of the atmosphere. In Section

12, we will discuss how to improve our atmospheric model in order to minimize the value of  $\Delta t_e = t_{0,mkf} - t_{0,e}$  for all energy bands.

Now, we will translate the results of Tables 5.1 and 5.2 into information about the spacecraft's position at  $t_0$ . Figure 5.6 shows a diagram that defines the relevant symbols and variables in our method to analyze the error in locating  $\mathbf{r}_{0,mkf}$ . The variables in Figure 5.6 are defined in Equation (29) through Equation (36).

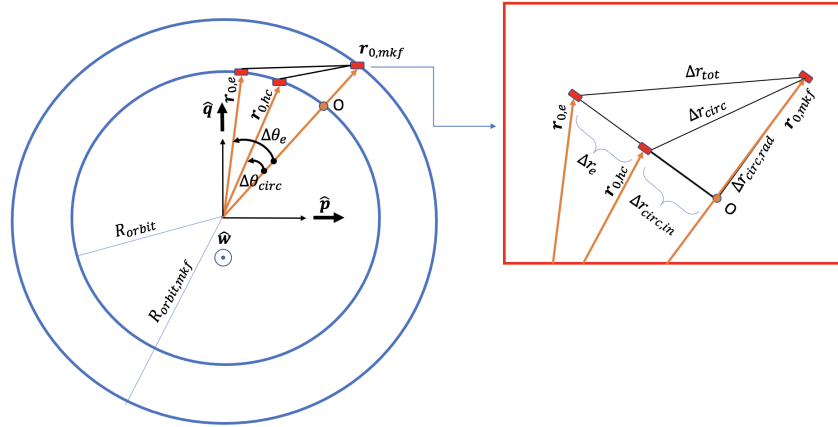


**Figure 5.6** This diagram shows the symbols and methods used to analyze the error of HCNM. We predict the satellite to be located at  $\mathbf{r}_{0,hc}$  at the time  $t_{0,e}$ , but if  $t_{0,e} \neq t_{0,mkf}$ , the predicted satellite orbit contains an extra source of in-track error,  $\Delta r_e$ . We introduce the position  $\mathbf{r}_{0,e}$  which can be compared to  $\mathbf{r}_{0,mkf}$  directly, since they both occur at the time  $t_{0,mkf}$ .  $R_{orbit}$  is the estimated orbital radius in our model, while  $R_{orbit,mkf}$  represents the instantaneous radius of the ISS orbit.

The total error in locating  $\mathbf{r}_{0,mkf}$  cannot be determined by comparing  $\mathbf{r}_{0,hc}$  and  $\mathbf{r}_{0,mkf}$  directly, since  $\mathbf{r}_{0,hc}$  is associated with the time  $t_{0,e}$ , while  $\mathbf{r}_{0,mkf}$  is associated with  $t_{0,mkf}$ . In order to compare the total error resulting from HCNM, we must consider the position vector  $\mathbf{r}_{0,e}$  that is associated with the time  $t_{0,mkf}$ . In this way, we can define  $\Delta r_{tot} = \mathbf{r}_{0,mkf} - \mathbf{r}_{0,e}$ . Later in this section, we will define the equation for  $\mathbf{r}_{0,e}$ , but for now, we will determine  $\Delta r_{tot}$  in an equivalent way by considering two different sources of error:  $\Delta r_{circ}$  between  $\mathbf{r}_{0,mkf}$  and  $\mathbf{r}_{0,hc}$ , as well as  $\Delta r_e$ , which is due to incorrectly identifying  $t_{0,e} = t_{0,mkf}$  in the horizon crossing. The first source of error,  $\Delta r_{circ}$ , is given by Equation (29):

$$\Delta r_{circ} = |\mathbf{r}_{0,hc} - \mathbf{r}_{0,mkf}|. \quad (29)$$

We call this the *geometrical* error due to the non-circularity of the ISS orbit, which we had assumed as perfectly circular in our method to locate  $\mathbf{r}_{0,hc}$  (Section 3.2.1). Moreover,  $\Delta r_{circ}$  can

be analyzed in terms of an *in-track* residual  $\Delta r_{circ,in}$ , and a *radial* residual,  $\Delta r_{circ,rad}$ , which are defined as follows:

$$\Delta r_{circ,rad} = |\mathbf{r}_{0,mkf}| - R_{orbit} \quad (30)$$

$$\Delta r_{circ,in} = R_{orbit} \Delta \theta_{circ} \quad (31)$$

$$\Delta \theta_{circ} = \theta_{0,hc} - \theta_{0,mkf} \quad (32)$$

where values  $\theta_{0,e}$  and  $\theta_{0,mkf}$  are defined as the in-track angular displacements (anomalies) of  $\mathbf{r}_{0,hc}$  and  $\mathbf{r}_{0,mkf}$  from the perigee of the ISS orbit. Therefore, we can define  $\theta_0$  (for either  $\mathbf{r}_0 = \mathbf{r}_{0,hc}$  or  $\mathbf{r}_0 = \mathbf{r}_{0,mkf}$ ) as follows:

$$\theta_0 = \tan^{-1} \frac{\mathbf{r}_0 \cdot \hat{\mathbf{q}}}{\mathbf{r}_0 \cdot \hat{\mathbf{p}}} \quad (33)$$

where  $\hat{\mathbf{q}}$  and  $\hat{\mathbf{p}}$  are the unit vectors that define the perifocal frame as described in ECI coordinates. The  $\Delta r_{circ}$  source of error is solely due to the non-circularity of the ISS orbit, and we calculated the same values of  $\Delta r_{circ}$ ,  $\Delta r_{circ,in}$ , and  $\Delta r_{circ,rad}$  when using both the model of Earth as an ellipsoid and as a sphere. For the case of the ISS orbit, we solved the following geometrical errors:

$$\Delta r_{circ} = 1.48 \text{ km}$$

$$\Delta r_{circ,in} = 1.38 \text{ km}$$

$$\Delta r_{circ,rad} = 0.51 \text{ km}.$$

Since  $\Delta r_{tot} = \Delta r_{circ}$  occurs when the atmospheric model causes no source of error ( $t_{0,e} = t_{0,mkf}$  is correctly located), we can say that  $\Delta r_{circ} = 1.48 \text{ km}$  is the “theoretical minimum” error in locating  $\mathbf{r}_{0,mkf}$  due to the non-circularity of the ISS orbit. In the notation of Figure 5.6, when  $t_{0,e} = t_{0,mkf}$ , the satellite position labeled  $\mathbf{r}_{0,e}$  lays on top of the satellite at  $\mathbf{r}_{0,hc}$ . However, as shown in Figure 5.6 and as we will see in the results of Table 5.3, when  $\Delta r_e$  is in the opposite direction of  $\Delta r_{circ,in}$  and  $|\Delta r_e| < 2|\Delta r_{circ,in}|$ , we will find that  $\Delta r_{tot} < \Delta r_{circ}$ . Therefore, we should define the “geometrical minimum” error as  $\Delta r_{circ,rad} = 0.51 \text{ km}$ , although this minimum occurs when there is a source of error in the atmospheric model. In this way, it is important to study the in-track error of the horizon crossing,  $\Delta r_e$ , separately from  $\Delta r_{tot}$  when analyzing the accuracy of our atmospheric model.

The error  $\Delta t_e = t_{0,mkf} - t_{0,e}$  is the in-track temporal error of the horizon crossing, and leads to the in-track positional error  $\Delta r_e$ . The equation for  $\Delta r_e$  is:

$$\Delta r_e = R_{orbit} \cdot \Delta \theta_e \quad (34)$$

$$\Delta \theta_e = \omega \cdot \Delta t_e. \quad (35)$$

Although this uncertainty represents an arc length, it is approximately a linear distance at the scale of an orbit, so it is a good estimate to draw the “error triangles” in Figure 5.6. Since

$\Delta r_e$  is a result of uncertainty in identifying  $t_{0,e} = t_{0,mkf}$ , it is an in-track source of error that can be attributed to error in the atmospheric model, as well as error in the model orbit. We define the total error as a superposition of the errors due to the circular orbit assumption and the in-track error in the measurement of the horizon crossing,  $\Delta r_e$ .

$$\Delta r_{tot} = \sqrt{(\Delta r_{circ,in} + \Delta r_e)^2 + \Delta r_{circ,rad}^2} \quad (36)$$

Equivalently, we can define  $\Delta r_{tot} = |\mathbf{r}_{0,e} - \mathbf{r}_{0,mkf}|$ , where  $\mathbf{r}_{0,e}$  is equal to  $\mathbf{r}_{0,hc}$ , but propagated an additional angular displacement of  $\Delta\theta_e = \omega\Delta t_e$  in its orbit:

$$\mathbf{r}_{0,e} = R_{orbit} \cdot (\cos(\theta_{0,hc} + \Delta\theta_e) \hat{\mathbf{p}} + \sin(\theta_{0,hc} + \Delta\theta_e) \hat{\mathbf{q}}) + 0 \hat{\mathbf{w}}. \quad (37)$$

Values of  $\Delta r_e$  and  $\Delta r_{tot}$ , and their corresponding standard errors are shown in Table 5.3. It is important to note that the standard error  $\delta t_e$  is equivalent to what we called  $\delta t_{hc}$  in Section 5.3.3, but we use the “e” subscript to emphasize that it is specific for a given energy band.

Oblate Earth Model				
Photon Energy Band	1.0 - 2.0 keV	2.0 - 3.0 keV	3.0 - 4.0 keV	4.0 - 5.0 keV
$\Delta t_e \pm \delta t_e$	$-0.12 \pm 0.13$ sec	$0.43 \pm 0.18$ sec	$0.44 \pm 0.27$ sec	$0.16 \pm 0.38$ sec
$\Delta r_e \pm \delta r_e$	$-0.92 \pm 1.02$ km	$3.30 \pm 1.40$ km	$3.37 \pm 2.06$ km	$1.23 \pm 2.90$ km
$\Delta r_{tot}$	0.65 km	4.64 km	4.72 km	2.60 km
Unattenuated Count Rate, $N_0$	251	91	42	18

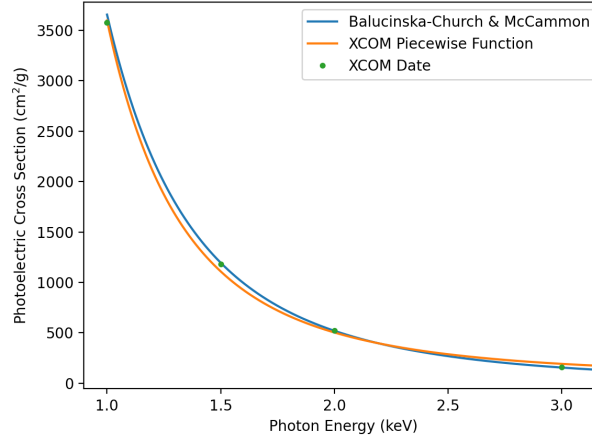
**Table 5.3** Error analysis of the V4641 Sgr. horizon crossing using a circular model orbit, a model of Earth as an ellipsoid, and the model of  $\sigma(E)$  given in Equation 19. The symbol  $\Delta r_{tot}$  represents the total error in locating  $\mathbf{r}_{0,mkf}$ , and  $\Delta r_e$  represents the part of the total error due to the horizon crossing measurement. The unattenuated count rate represents the average number of counts per 1 second bin at the top of a transmittance curve.

Table 5.3 shows the error analysis involved in locating the ISS at  $\mathbf{r}_{0,mkf}$  for five energy bands from 1 – 5 keV. The values  $\Delta r_{tot}$  indicates our total error of locating the ISS in our version of the *cool start* problem, and  $\Delta r_e$  shows the in-track accuracy of HCNM, which provides direct insight into the accuracy of our atmospheric model. Values of  $\Delta r_e$  for all energy bands except 2.0 – 3.0 keV are consistent with zero at two standard errors, while the 2.0 – 3.0 keV is consistent at 2.4 standard errors. Table 5.3 can be compared to Table A.1, which is re-printed from Ruhl et al. (2022); however Table 5.3 uses a piecewise model of  $\sigma(E)$ , as well as a circular orbit model when calculating the transmittance curves used for HCNM. On the other hand, all results in Table A.1 are consistent with zero at one standard error. In the results of Table A.1, the known positions from the mkf-extension file and  $\sigma(E)$  from Balucinska-Church and McCammon (1992) (which we will call BCMC moving forward) were used when calculating transmittance curves, both of which are more precise than the method used in this paper for the cool start scenario. Specifically, error in the piecewise model of  $\sigma(E)$  plays the major role in the larger errors of

Table 5.3, as the relationship that  $\sigma(E) \propto E^{-3}$  is not perfect. The photo-electric cross sections fits from BCMC are exponential models with more parameters that were fit to many more data points than we used when constructing the piecewise model of Equation (19). Table A.2 shows the results of the V4641 Sgr. crossing when using the circular orbital model and the BCMC cross sections, thus showing more directly the effect the circular model, as there is no extra error caused by the cross sections.

It is also important to note that the standard errors, which represent the amount of time necessary to make the  $\chi^2$  between the model and data transmittance curves increase by one, are very similar to the standard errors of Table A.1, which uses cross sections from BCMC. This supports our previous statement that the value of  $\sigma(E)$  mainly corresponds to shifting the transmittance model left and right and does not affect the quality of the comparison with the data, which is indicated by  $\delta t_{hc}$ .

The positive or negative sign of  $\Delta r_e$  also provides insight into our atmospheric model. In general,  $\Delta r_e < 0$  means that our atmospheric model is too “thick”, or we predict the transmittance curve to rise too late in time because of error in the orbital model. As compared to the results in Table A.1, since the same model of  $\rho(z)$  is used, we expect that  $\sigma(E)$  in the piecewise model is smaller than the BCMC model for the 1.0 – 2.0 keV energy band, and larger than BCMC above  $\sim 2$  keV, which is the relationship shown in Figure 5.7. In the conclusion, we will further discuss what the sign of  $\Delta r_e$  can tell us about our model of absorption cross section for the 0.3 - 1.0 keV energy band.



**Figure 5.7** BCMC fits of photo-electric cross section plotted against the piecewise  $\sigma(E) \propto E^{-3}$  function, which is fit to the XCOM data points in green. The BCMC cross sections are much more accurate than the piecewise model, as they are fit to more data and use a more complicated functional form.

For the energy bands above 2.0 keV, the error analysis looks similar to the triangle shown

in Figure 5.6;  $\Delta t_e > 0$ , thus producing a value of  $\Delta r_e$  that is in the same positive direction as  $\Delta r_{circ}$ . The 1.0 – 2.0 keV energy band has  $\Delta r_e < 0$ , so the two triangles in Figure 5.6 change, as the red box (satellite) representing  $\mathbf{r}_{0,e}$  would move to the opposite side of  $\mathbf{r}_{0,hc}$ . In the column for 1.0 – 2.0 keV, we see that  $\Delta r_e$  partially cancels out with  $\Delta r_{circ}$ , thus producing a  $\Delta r_{tot}$  that can be less than the theoretical minimum of  $\Delta r_{circ}$ . Table A.2 shows the results of the V4641 Sgr horizon crossing when the BCMC cross sections are used instead of the piecewise model. Both Tables use the circular orbit model. The results of Table A.2 are more accurate for all energy bands, and are consistent with zero at less than 1.35 standard errors, as compared to 2.4 standard errors in Table 5.3.

### 5.5.3 Navigational Scenario: Spherical Earth Approximation

In a real navigational scenario, we may not know certain information about the orbited planet, such as the exact shape of the planet or certain aspects of the atmospheric model. Therefore, it is extremely important to understand how these “limiting” scenarios affect the accuracy of the Horizon Crossing Navigational Method. In this section, we will assume that we only know the volumetric mean radius of earth,  $R_{earth} = 6371.0$  km, instead of its description as an ellipsoid. Table 5.4 below:

Spherical Earth Model	
$t_{0,mkf}$	368.23 sec
$\mathbf{r}_{0,mkf}$ (km)	[-4512.24, 3838.19, -3331.05]
$\mathbf{r}_{0,hc}$ (km)	[-4513.63, 3836.89, -3331.73]

**Table 5.4** Values of  $t_{0,mkf}$ ,  $\mathbf{r}_{0,mkf}$ , and  $\mathbf{r}_{0,hc}$  calculated for a spherical earth. Uncertainties in each vector component corresponding to the (0.01 second) time steps of our numerical model orbit are  $x \pm 0.01$ ,  $y \pm 0.03$ , and  $z \pm 0.03$ .

Comparing the values of  $t_{0,mkf}$  for both spherical and oblate earth models, we can see an interesting geometric phenomenon: NICER’s line of sight is tangent to the earth 1.05 seconds earlier when considering the earth as an oblate spheroid as compared to a perfect sphere. Since the ISS travels at a linear velocity of about 7.6 km/sec, we expect that the spherical approximation may lead to values of  $\mathbf{r}_0$  that could be about 8 km less accurate than the oblate earth model.

Comparing the calculated transmittance curves to the X-ray data, we determined values of  $t_{0,e}$ , and subsequently performed the same error analysis as was done in Section 5.5.2. The results of  $t_{0,e}$ ,  $\Delta r_{circ}$ , and  $\Delta r_e$  are shown in Table 5.5:

Spherical Earth Model				
Photon Energy Band	1.0 - 2.0 keV	2.0 - 3.0 keV	3.0 - 4.0 keV	4.0 - 5.0 keV
$\Delta t_e \pm \delta t_e$	$1.11 \pm 0.13$ sec	$1.64 \pm 0.18$ sec	$1.66 \pm 0.25$ sec	$1.39 \pm 0.39$ sec
$\Delta r_e \pm \delta r_e$	$8.50 \pm 1.00$ km	$12.56 \pm 1.39$ km	$12.71 \pm 1.88$ km	$10.64 \pm 2.98$ km
$\Delta r_{tot}$	9.84 km	13.89 km	14.04 km	11.98 km

**Table 5.5** Error analysis of the V4641 Sgr. horizon crossing using a circular model orbit, a model of Earth as a sphere, and the model of  $\sigma(E)$  given in Equation 19.  $\Delta r_{tot}$  represents the total error in locating  $\mathbf{r}_{0,mkf}$  (the “best estimate” of position if it is only known that Earth is a sphere), and  $\Delta r_e$  represents the part of the total error due to the atmospheric model.  $\Delta r_e$  is a result of  $\Delta t_e$ .

As expected, the values of  $\Delta r_e$  and  $\Delta r_{tot}$  are larger than for the model of earth as an ellipsoid. Moreover, since all values of  $\Delta t_e$  are greater than zero, each of the energy bands predict a start of the horizon crossing that occurs too early in time, as both  $\Delta r_e$  and  $\Delta r_{circ}$  are positive. The results for the spherical approximation are less accurate than the ellipsoid model across the board. The values of  $\delta t_{hc}$  are the same as those when using the ellipsoid Earth model (Table 5.3) for the 1.0 – 2.0 keV and 2.0 – 3.0 keV energy bands, and slightly different for the 3.0 – 4.0 keV and 4.0 – 5.0 keV bands. This indicates that using a spherical model of Earth to calculate the shape of transmittance curves works very well. For this reason, the assumption of a “spherically stratified” atmosphere is often used when analyzing atmospheric occultations. Spherical symmetry is a fundamental assumption of the method for density retrieval introduced by Roble and Hays (1972), as it involves “inverting” the Abel integral, a technique that is often used in geometrical optics. However, the shape of the higher energy data curves, which come through at lower altitudes (90 – 100 km), may be slightly affected by the oblateness of Earth’s atmosphere which is not captured when we make the spherical Earth approximation. At altitudes above 100 km in which 1.0 – 2.0 keV and 2.0 – 3.0 keV X-rays are transmitted, the atmosphere is spherically stratified to an even greater extent than in the altitude range of 90 – 100 km. When analyzing higher energy X-rays that are transmitted below 90 km, the approximation of a spherically symmetric atmosphere becomes less accurate. Alternatively, this small difference in  $\delta t_{hc}$  could be present for all energy bands, but only appear above 3.0 keV, a range in which V4642 Sgr. emits a much smaller number of X-ray counts.

#### 5.5.4 Weighted Mean of Results

In order to determine the most accurate measurement from a horizon crossing, we can take the weighted mean of the results from the four energy bands. In practice, taking the weighted mean is a method of combining the four results of  $t_{0,e} \pm \delta t_{0,e}$  into a single value of  $t_0 \pm \delta t_0$  which will, from a statistical perspective, always be more accurate. This value of  $t_0$  could then be inputted into a navigational filter with a measurement uncertainty of  $\delta t_0$ . We will demonstrate this method with the values of  $\Delta t_e$  in order to determine the overall in-track accuracy attainable in the cool start

problem. The weighted means are calculated for  $\Delta t_{hc} \pm \delta t_{hc}$ , and values of  $\Delta r_{hc} \pm \delta r_{hc}$  will be determined by multiplying the times by the ISS's orbital velocity at  $\mathbf{r}_0$ ,  $v_0 \sim 7.65$  km/sec. The weights for each energy band,  $w_e$ , are proportional to the inverse of the standard error squared

$$w'_e = \frac{1}{\delta t_e^2} \quad (38)$$

$$w_e = \frac{w'_e}{\sum_e w'_e}, \quad (39)$$

where the values of  $w_e$  are normalized so that they add to one. The weighted mean of  $\Delta t_e$  and the corresponding standard error are given by the following equations:

$$\Delta t_{hc} = \sum_e w_e \Delta t_e \quad (40)$$

$$\delta t_{hc}^2 = \sum_e (w_e \delta t_e)^2. \quad (41)$$

By averaging the results of Tables 5.3 and 5.5, we can determine the overall in-track temporal and positional accuracy achieved from the horizon crossing using the model of Earth as an ellipsoid and as a sphere. The weighted means are shown in Table 5.6 below.

Weighted Mean	Ellipsoid Earth	Spherical Earth
$\Delta t_{hc} \pm \delta t_{hc}$	$0.12 \pm 0.09$ sec	$1.35 \pm 0.09$ sec
$\Delta r_{hc} \pm \delta r_{hc}$	$0.92 \pm 0.72$ km	$10.34 \pm 0.72$ km

**Table 5.6** Weighted means of the results of the V4641 Sgr. horizon crossing in the cold start scenario. This table shows the weighted means of the results of Tables 5.3 and 5.5.

The weighted mean of the “non-cold-start” scenario results with the ellipsoidal Earth (Table A.1) are  $0.60 \pm 0.80$  km, as reported by Ruhl et al. (2022), which agree at one standard error. In comparison, the cold-start results are  $0.92 \pm 0.72$  km and are consistent with zero at  $\sim 1.3$  standard errors, as they contain additional error from the circular orbital model (up to 2km during the horizon crossing) as well as a less precise model for atmospheric cross section. Even though there is additional uncertainty going into the horizon crossing, the value of  $\delta t_{hc}$  does not increase accordingly (it is actually smaller by 0.06 sec). Therefore, the  $\chi^2 + 1$  criterion is not sensitive to the quality of the comparison between the model transmittance curve and the binned X-ray data. For this reason, when we expect that there is uncertainty in the orbital model or atmospheric model before the horizon crossing, the estimated measurement uncertainty should be scaled or adjusted accordingly. Table 5.6 also shows that the  $\chi^2 + 1$  criterion is not sensitive to uncertainty in the Earth’s shape, as the standard errors are equal for both the spherical and ellipsoidal models of Earth. In Part II, we will gain insight into the extent to which these standard errors should be adjusted when there are different types of error in the horizon crossing model.

## Part II: Simulations and Error Budget of HCNM

As shown in Ruhl et al. (2022), HCNM can provide in-track position correction with accuracies of  $< 1$  km depending on the brightness of a source, the accuracy of the input orbital model, and the accuracy of the atmospheric model. In Part I of this paper, it was shown that knowing the shape of Earth is very important in HCNM. We also saw that, when HCNM is applied to an approximately circular orbit and when a simplified model for atmospheric cross section is used, HCNM can still provide reliable in-track measurements, but the estimated measurement uncertainties may need to be adjusted when there are these extra sources of error. These two demonstrations not only provide a “proof of concept”, but also show that HCNM can provide a reliable input to a navigational filter, specifically for a satellite in an approximately circular orbit around a planet that has a well-defined shape and atmospheric model.

In a deep-space navigational scenario navigating around a distant planet, these factors that affect the performance of HCNM in Earth orbit, such as uncertainty in the input orbit model and uncertainty in the orbited planet’s atmospheric model, will be even larger. The goal of Part II of this paper is to present a couple preliminary simulations of HCNM to help us better understand its *error budget*. We will explore how uncertainties in the velocity of the input orbit model, uncertainties in the total atmospheric cross section and composition, and uncertainties in the position of the telescopic “grazing point” affect the reliability of HCNM measurements. Knowledge of the out-of-plane angle and the atmospheric density model are also important aspects of the error budget, and are starting to be explored quantitatively (Hladky, 2022). We are currently developing simulators to simulate HCNM for different orbital models and different X-ray sources (Schwab, 2022), and the preliminary case studies in Part II will provide inspiration for future in-depth simulations.

## 6 Two NICER Horizon Crossings

The horizon crossing of V4641 Sgr. was detected on February 3, 2020, and on August 11, 2021, NICER detected another horizon crossing of the Crab Nebula. During this horizon crossing, NICER did not “lock-on” to the Crab Nebula until about 40 seconds into the horizon crossing, which affected portions of the detected transmittance data, especially the higher energy bands that start to come in before 40 seconds (Ruhl et al., 2022). As shown by Ruhl et al. (2022), it is possible to account for a late-lock by only analyzing the portion of the data that is unaffected by the late-lock. For this reason, in Sections 10 and 11, when the horizon crossing of the Crab Nebula is considered, a “comparison window”, is specified, rather than simply using the default 1% – 99% Ruhl et al. (2022). In contrast to the results of Part I which use a circular input orbital model, the results produced by Ruhl et al. (2022), which are re-printed in Appendix A, are created with an orbital model from NICER’s “mkf” file, a file which contains GPS measurements corrected for NICER’s position on the ISS. This must be considered when comparing the results of different results tables.

In Part II, we continue to use the notation in which the uppercase  $\Delta$  is the error in locating  $t_0$  or  $\mathbf{r}_0$  as compared to the “mkf” position data, whereas the lowercase  $\delta$  represents the “standard error” which is related to the brightness of the source and the number of data points included in the comparison.

## 7 Orbital Velocity

In this section, we simulate the a situation in which we overestimate or underestimate the orbital velocity of the input model and calculate the position of the ISS using the misestimated velocity. Since this analysis is done for the orbital scenario of the V4641 Sgr. horizon crossing, these results correspond to an out-of-plane angle of  $\psi = -2.59^\circ$ . In this way, the analysis presented here will be slightly different for a different angle  $\psi$ , but the general trend will be the same. We used linear orbital velocities,  $v = \omega R_{orbit}$ , between 7.26 km/sec and 8.06 km/sec, where  $\sim 7.66$  km/sec is the actual orbital velocity of the ISS during the horizon crossing. In order to directly evaluate the effects of a change in orbital velocity, we keep  $R_{orbit}$  constant. Therefore, the model orbits are not consistent with Kepler’s Third Law (Equation 21), but will enable us to see the effects of changing orbital velocity, without changing the length of the line of sight used in the analysis. As shown in Figure 7.1, when orbital velocity increases, the altitude of the tangent point on the line of sight, or simply the tangent altitude, increases more quickly. Therefore, the ISS reaches the “end” of the horizon crossing more quickly, which can be seen in Figure 7.1, as the different color curves end at different times.

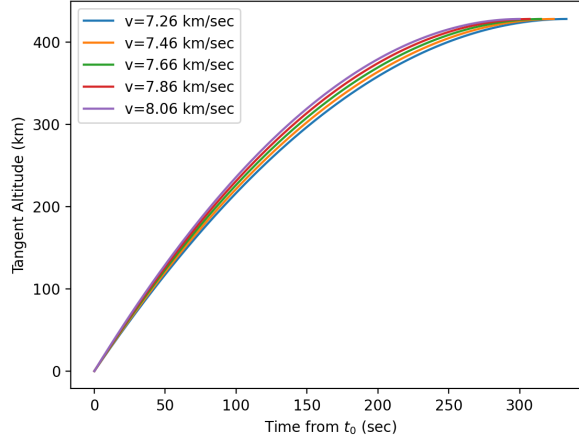


**Figure 7.1** Tangent altitude increases more rapidly with time when the ISS moves at a faster orbital velocity.

In the case where the misestimated orbital velocity is too large, since the satellite’s line of sight is modeled to penetrate higher-than-actual tangent altitudes, we erroneously predict the

model atmosphere to be thinner than it actually is. Therefore, the transmittance curve rises sooner in time than the actual data. This can be seen in Figure 7.2a, where the purple curve corresponding to  $v = 8.06$  km/sec, rises before the models that use slower orbital velocities. Since changing the orbital velocity only slides the curves left and right and does not affect the quality of the comparison with the data points, we compare each of the models to the green curve at  $v_{0,best} = 7.66$  km/sec  $\approx v_{0,mkf}$ . Because of this left-right shift, only the error  $\Delta r_0$  will be affected, and the  $\chi^2 + 1$  measurement uncertainty,  $\delta r_0$ , will stay approximately constant. Figure 7.2b shows that the transmittance vs tangent altitude curve stays the same when orbital velocity is changed. Transmittance as a function of tangent altitude is a property of a planet's atmosphere, and will always be approximately the same between observations around the same planet (even for different satellites), provided that the atmosphere has not changed significantly.

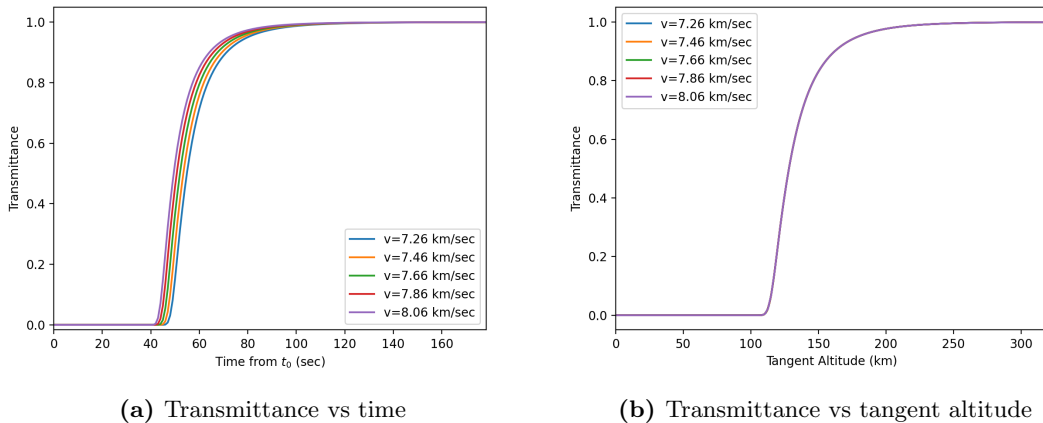


**Figure 7.2** Transmittance curves when altering orbital velocity for the 2.0 – 3.0 keV energy band. The transmittance models correspond to the circular orbit model on the day of the V4641 Sgr. horizon crossing.

Figure 7.3 shows the in-track error,  $\Delta r_0$  resulting from using an incorrect orbital velocity with an error of  $\Delta v_0 = v - v_{0,best}$ . The in-track error,  $\Delta r_0$ , is defined as

$$\Delta r_0 = |\mathbf{v}_{0,mkf} \cdot \Delta t_{50}| \quad (42)$$

where  $v_{0,mkf}$  is the velocity at the start of the horizon crossing from the mkf-extension file and  $\Delta t_{50}$  is the amount of time that the curve corresponding to  $\Delta v_0$  is shifted from the  $v = 7.66$  km/sec transmittance curve, as measured between the “50% transmission” points. The error in the orbital velocity  $\Delta v_0$  is plotted on the x axis of Figure 7.3, and the same analysis is repeated each of the four energy bands from 1.0 to 5.0 keV.

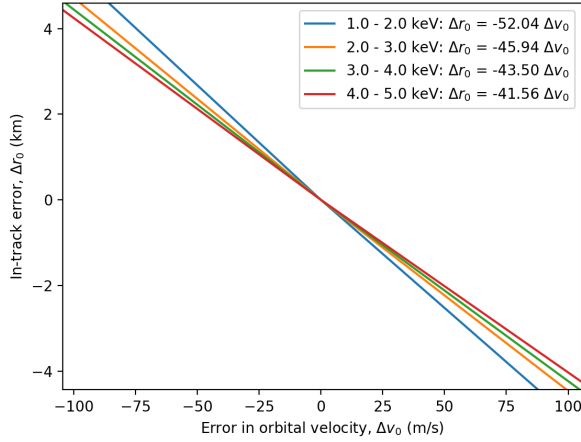


**Figure 7.3** In-track error as a function of error in orbital velocity for different X-ray energy bands.

Figure 7.3 shows that the lower energy bands are more affected by an error in orbital velocity. This makes sense because the transmittance curves of the lower energy bands take a longer time to rise from 0% to 100%, and thus are affected by the error in velocity for a longer period of time than the higher energy bands. If we expect that there is a significant error in our model of orbital velocity, it is important to know that the lower energy bands will be slightly less reliable. In the case of the weighted sum of results, relatively less weight can be applied to the results from the lower energy bands.

Overall, Figure 7.3 shows that in order to achieve an in-track position measurement that is not systematically shifted by  $\sim 4$  km, orbital velocity must be known to  $\sim 100$  m/s. In order to achieve an in-track measurement accurate to  $\sim 1$  km, orbital velocity must be known to 25 m/s. Although this analysis was done for a circular orbit, the results provide good insight into how well a more elliptical orbit must be known in order to correctly predict a transmittance curve.

## 8 Atmospheric Cross Section

Ruhl et al. (2022) consider the performance of HCNM when a pure oxygen or pure nitrogen cross section is used as the model of the total cross section of attenuation,  $\sigma(E)$ . For the 1.0 – 2.0 keV energy band, the pure nitrogen cross section is  $\sim 7\%$  smaller than the expected three-element mix (78% N, 21% O, 1% Ar), and the pure oxygen cross section is  $\sim 30\%$  larger than the expected cross section. The nitrogen approximation leads to a 2 km in-track error and the oxygen approximation leads to a  $-8.5$  km in-track error (Ruhl et al., 2022). In this paper, we present a more general analysis where we scale the expected cross section,  $\sigma_{best}(E)$ , by the multiplicative factor  $\alpha$  for each energy band. Similar to the error in orbital velocity, an error in cross section

shifts the transmittance curve left and right on the time axis, while atmospheric density and a source's spectrum more strongly determine the shape of a transmittance curve. However, since the atmospheric model is different when altering  $\sigma(E)$ , the model curve of transmittance vs tangent altitude also changes (unlike Figure 8.1), which is shown in Figure 8.1. Figure 8.2 shows a plot of  $\Delta r_0$  (Equation 42) plotted against the cross section scaling factor,  $\alpha$ .

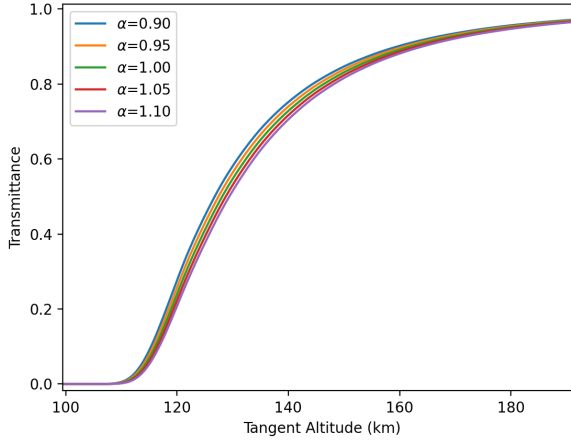


**Figure 8.1** Curves of transmittance vs tangent altitude slide to the left or right on the time axis when cross section is altered and the same density model is used.

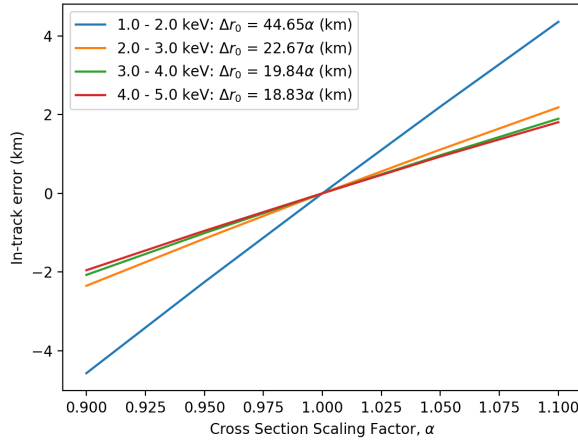


**Figure 8.2** In-track error versus scaling factor,  $\alpha$ , of the atmospheric cross section.

Figure 8.2 clearly shows that the 1.0 – 2.0 keV energy band is less reliable when we expect that there is an error in the model of atmospheric cross section. This finding is similar to the

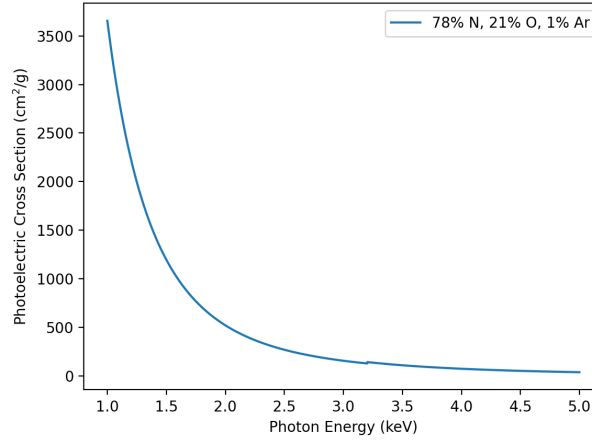


**Figure 8.3** Photo-electric cross section as a function of Energy. Cross sections retrieved from Balucinska-Church and McCammon (1992).

results of the velocity simulation in Figure 7.3, and it may also be related to the fact that the horizon crossing of the 1.0 – 2.0 keV band takes longer in time, but overall it is caused by a different mechanism. We expect this to be related to the fact that photo-electric the variation of cross section is significantly larger in the 1.0 – 2.0 keV energy band than in the other bands, as  $\sigma(E) \propto E^{-3}$ . Figure 8.3 shows a plot of the total cross section versus energy for the model of Earth’s atmosphere used in this paper.

## 9 Effective Transmittance Model

The  $E^{-3}$  functional dependence of the photoelectric cross section on photon energy,  $E$ , is also the reason that we use the “effective transmittance” model in Equation (26). Since  $\sigma(E)$  changes so much within a single energy band, especially below 3 keV, it is necessary to break up the 1 keV energy band into smaller steps of size  $dx$ . Table 9.1 displays some the values from Figure 8.3, where  $\Delta\sigma = \sigma_1 - \sigma_2$ , where  $\sigma_1$  at  $E_1$  is the value of cross section on the left side of the energy band and  $\sigma_2$  at  $E_2$  is the cross section on the right side of the energy band.

Energy Band	$\Delta\sigma$ (cm <sup>2</sup> /g)	$\Delta\sigma/\sigma_1$
1.0 – 2.0 keV	3136	0.86
2.0 – 3.0 keV	365	0.70
3.0 – 4.0 keV	82	0.53
4.0 – 5.0 keV	36	0.49

**Table 9.1** Drop in atmospheric cross section within individual energy bands from 1.0 – 5.0 keV. The values in this table are determined from Table 8.3.

Figure 9.1 shows a plot of 1.0 – 2.0 keV transmittance curves calculated with multiple values of  $dx$  plotted against data from the Crab Nebula horizon crossing. The plot shows that the effective transmittance model is important for the 1.0 – 2.0 keV energy band, as it helps the model better predict the shape of the data. Specifically, the curve with  $dx = 0.25$  keV best models the data, and a smaller step size in energy is a waste of computation time. Figure 9.2 shows a portion of the transmittance curve for 2.0 – 3.0 keV, which shows that  $dx = 0.5$  keV is sufficient to predict the shape of the data. For the two energy bands above 3.0 keV, the curves that use  $dx < 1$  keV are approximately equal to the curve that uses  $dx = 1$  keV.

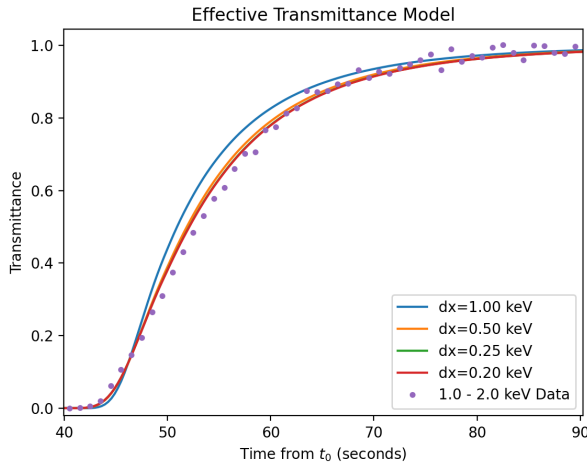


**Figure 9.1** Transmittance model curve compared to binned photon events from the Crab Nebula horizon crossing. This plot shows that an “effective transmittance” model with steps of  $dx=0.25$  keV within the 1.0 – 2.0 keV energy band is needed in order to best fit the shape of the data.

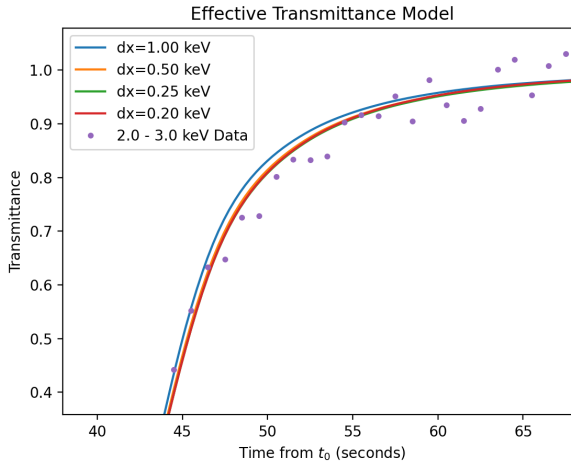


**Figure 9.2** Effective transmittance model curves for 2.0 – 3.0 keV photons compared to data from the Crab Nebula. The plot shows that  $dx=0.5$  keV is needed to best fit the shape of the data.

It is important to know that the effective transmittance model is not necessary for energy bands above 3 keV, as eliminating this step from the calculation can save computation time on a flight computer. For example, the calculation of a single transmittance curve for an energy band with a width of 1 keV using  $dx = 1.0$  keV takes about 4 seconds using Python, but if  $dx = 0.25$  keV is used, then the calculation will take nearly 16 seconds. Moreover, many of the candidate X-ray sources for horizon crossings are strong emitters below 3 keV, such as V4641 Sgr and the Crab Nebula. In order to maximize the amount of useable data and reduce error, it is important to correctly model below 3 keV with the effective transmittance model.

## 10 Importance of Argon

Below an altitude of 85 km, the average volumetric mix of Earth’s atmosphere is 78% N<sub>2</sub>, 21% O<sub>2</sub>, and 1% Ar. Although this ratio changes above 85 km, this simple ratio seems to work very well for HCNM. Since the abundance of argon decreases above 85 km, and even reaches  $\sim 0.2\%$  at 130 km, one may ask if it is necessary to include argon at all in the atmospheric model. Determan et al. (2007) note that, despite the small abundance of argon, the 1.0% should be included in analyses because the cross section of argon is up to an order of magnitude larger than that of N and O in portions of the analyzed energy pass band. Specifically, above argon’s k-edge at 3.2 keV, we expect that argon will play a significant role in X-ray absorption. Figure 10.1 shows a plot of cross sections of N, O, and the three element mix as functions of energy. Even though the mix only contains 1% argon, the k-edge appears as a sharp jump in cross section and X-ray absorption.

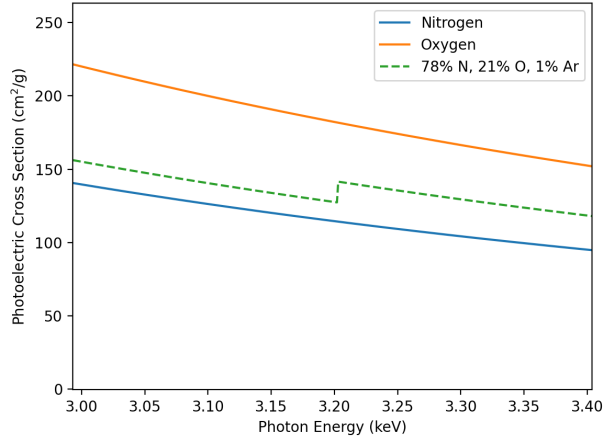


**Figure 10.1** Plot of elemental photo-electric cross sections as a function of photon energy (Balucinska-Church and McCammon, 1992).

In order to understand the sensitivity of HCNM to the presence of argon, we repeated the analysis of the two horizon crossings when using an atmospheric cross section of 78% N and 22% O in Tables 10.1 and 10.2. These results tables do not use the circular model orbit, but rather they use the orbital solution from the mkf-extension file in the calculation of the model transmittance curve. In this way these results reduce any inaccuracies caused by the input orbit model, and therefore, the results should be compared with Tables A.1 and A.3.

Energy Band	1.0 – 2.0 keV	2.0 – 3.0 keV	3.0 – 4.0 keV	4.0 – 5.0 keV
$\Delta t_{hc} \pm \delta t_{hc}$ (sec)	$0.07 \pm 0.15$	$0.15 \pm 0.18$	$0.07 \pm 0.28$	$-0.22 \pm 0.44$
$\Delta r_{hc} \pm \delta r_{hc}$ (km)	$0.54 \pm 1.11$	$1.15 \pm 1.38$	$0.54 \pm 2.13$	$-1.68 \pm 3.37$
Full Transmit (counts)	244.0	89.0	39.9	18.6

**Table 10.1** Results of the V4641 Sgr. horizon crossing when using an atmospheric cross section consisting of 78% N and 22% O. The “mkf” positions and BCMC cross sections are used in the calculations of these results.

Energy Band	1.0 – 2.0 keV	2.0 – 3.0 keV	3.0 – 4.0 keV	4.0 – 5.0 keV
Time Range	44.0 - 98.0 sec	41.0 – 76.0 sec	41.0 – 65.0 sec	41.0 – 58.0 sec
Transmittance Range	1.0% – 99.0%	3.8% – 99.0%	25.6% – 99.0%	51.6% - 99.0%
$\Delta t_{hc} \pm \delta t_{hc}$ (sec)	$0.06 \pm 0.03$	$0.08 \pm 0.05$	$-0.42 \pm 0.09$	$-0.28 \pm 0.07$
$\Delta r_{hc} \pm \delta r_{hc}$ (km)	$0.46 \pm 0.21$	$0.61 \pm 0.41$	$-3.21 \pm 0.72$	$2.14 \pm 0.58$
Full Transmit (counts)	5378	1406	584	275

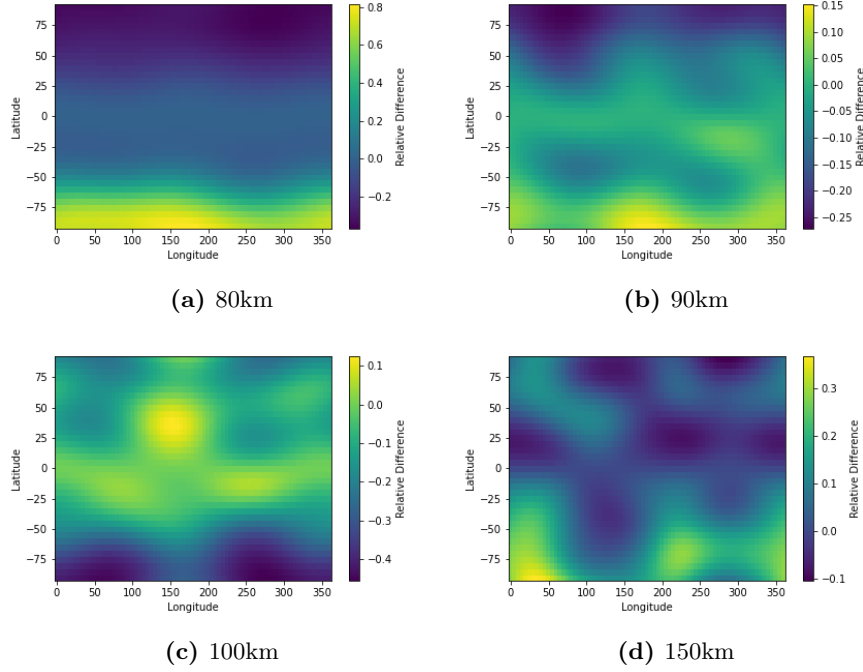
**Table 10.2** Results of the Crab Nebula horizon crossing when using an atmospheric cross section consisting of 78% N and 22% O. The “mkf” positions and BCMC cross sections are used in the calculations of these results.

For the V4641 Sgr horizon crossing, three values of  $\Delta_{hc}$  are not consistent with zero within  $\sim 2$  standard errors,  $\delta_{hc}$ . In the results for the Crab Nebula in Table 10.2, we also see that the 2-element mix is statistically worse than the 3-element mix, as  $\Delta_{hc} < \delta_{hc}$  for all energy bands. The measurements from the 1.0 – 2.0 and 2.0 – 3.0 keV bands are consistent with the “mkf” truth standard to about two standard errors, but the 3.0 – 4.0 and 4.0 – 5.0 keV bands both show disagreement to more than 3.5 standard errors. This disagreement is, in part, because the lower energies are transmitted through the atmosphere at higher altitudes where there is < 1.0% argon, and also because argon is a significant contributor to the total X-ray absorption in the atmosphere above its k-edge at 3.2 keV.

## 11 Importance of Longitude and Latitude

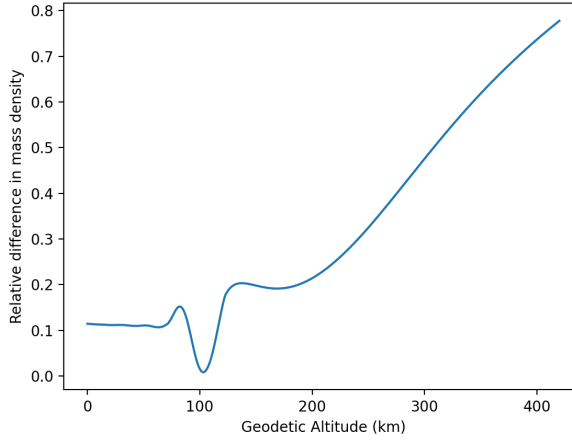
Throughout this paper, we have assumed that we were able to identify both the latitude and longitude of the “grazing point”, which are used as inputs into the MSIS atmospheric model when extracting density profiles as a function of altitude (all inputs to the MSIS model can be found in Table B.1 of Appendix B). However, when navigating around an unknown planet, it may only be possible to determine the latitude of the grazing point. The longitude could only be determined if we were to define an equivalent of the Greenwich Meridian on the unknown planet. For this reason, it is important to understand the sensitivity of HCNM to an atmospheric density model that does not include longitudinal information.

Figure 11.1 shows MSIS-00 models of atmospheric density, plotted as a relative (fractional) difference from equatorial density, as a function of latitude and longitude on the day of the V4641 Sgr. horizon crossing. The subfigures show density maps at four altitudes: 80 km, 90 km, 100 km, and 150 km. We show the heat plots at different altitudes because different energy photons penetrate Earth’s atmosphere at different altitudes.



**Figure 11.1** Mass Density in Earth’s atmosphere, plotted as relative difference from equatorial density.

These plots show that the atmosphere is less “layered” at higher altitudes. Since the plots are created for the date of the V4641 Sgr. horizon crossing in February of 2020, the latitudinal and longitudinal variation of density does not always look like this. Nevertheless, this layering at lower altitudes is a general trend with atmospheric density on Earth. Latitudinal variations in thermospheric density are mainly driven by seasonal variations of solar irradiance, geomagnetic heating at high latitude, and other internal dynamics Qian and Solomon (2012). Longitudinal variations, on the other hand, are less significant than latitudinal variations, and are associated with variations in electron density (conductance), Joule heating, and auroral heating Qian and Solomon (2012). Based on Figure 11.1, we expect that knowing the instantaneous longitude will affect the results of the lower energy bands more than the higher energy bands. In order to estimate the sensitivity of HCNM to the longitude of the grazing point, we average the density profile over  $360^\circ$  of longitude (at  $40^\circ$  intervals) at a known latitude when calculating the density profile that is used in the atmospheric model. Figure 11.2 plots the fractional difference between the density profile defined at the latitude and longitude of the grazing point ( $-43.26^\circ$  latitude and  $90.28^\circ$  longitude) and the longitudinally-averaged profile for the V4641 Sgr observation, and shows that the difference between the two profiles increases with increasing altitude. Figure 4.1 of Appendix D shows the plots of the two density profiles as a function of altitude.



**Figure 11.2** Difference between the MSIS-00 longitudinally-averaged density profile and the density profile defined at the grazing point.

Tables 11.1 and 11.2 below show the expected relationship that the lower energy bands are more affected by uncertainty in the longitude of the grazing point. The 4.0 – 5.0 keV band from the Crab horizon crossing does not agree with the general trend, since it still agrees with zeros within two standard errors. This disagreement could be a result of trimming the comparison time range of the Crab horizon crossing, as there are only 17 data points in the comparison.

Energy Band	1.0 – 2.0 keV	2.0 – 3.0 keV	3.0 – 4.0 keV	4.0 – 5.0 keV
$\Delta t_{hc} \pm \delta t_{hc}$ (sec)	$0.73 \pm 0.17$	$0.33 \pm 0.20$	$0.33 \pm 0.27$	$0.09 \pm 0.39$
$\Delta r_{hc} \pm \delta r_{hc}$ (km)	$5.59 \pm 1.31$	$2.53 \pm 1.56$	$2.53 \pm 2.07$	$0.69 \pm 2.96$
Unattenuated Counts, $N_0$	244	89	40	19

**Table 11.1** Results of the V4641 Sgr horizon crossing using a density profile that is averaged over all longitudes

Energy Band	1.0 – 2.0 keV	2.0 – 3.0 keV	3.0 – 4.0 keV	4.0 – 5.0 keV
Time Range	44.0 – 98.0 sec	41.0 – 76.0 sec	41.0 – 65.0 sec	41.0 – 58.0 sec
Transmittance Range	1.0% – 99.0 %	3.8% – 99.0%	25.6% – 99.0%	51.6% – 99.0%
$\Delta t_{hc} \pm \delta t_{hc}$ (sec)	$0.56 \pm 0.03$	$0.29 \pm 0.05$	$0.04 \pm 0.10$	$0.64 \pm 0.49$
$\Delta r_{hc} \pm \delta r_{hc}$ (km)	$4.28 \pm 0.27$	$2.22 \pm 0.38$	$0.31 \pm 0.76$	$4.90 \pm 3.73$

**Table 11.2** Results for the Crab Nebula horizon crossing using a longitudinally-averaged density profile.

The weighted mean results of Tables 11.1 and 11.2 are shown in Table 11.3 below.

Weighted Mean	Crab	V4641 Sgr.
$\Delta t_{hc} \pm \delta t_{hc}$	$0.46 \pm 0.02$ sec	$0.48 \pm 0.11$ sec
$\Delta r_{hc} \pm \delta r_{hc}$	$3.53 \pm 0.19$ km	$3.70 \pm 0.86$ km

**Table 11.3** Weighted means of HCNM results when using a density profile averaged over all longitudes (Tables 11.1 and 11.2).

These results emphasize that the  $\chi^2 + 1$  uncertainty criterion does not adjust for the quality of a fit, as the standard errors are approximately equal to those in Table 5.6 and Table A.1. In fact, for a source as bright as the Crab Nebula, the values of  $\delta$  may give an unrealistic confidence level in a measurement. Therefore, for a horizon crossing around Earth, or another planet which has considerable longitudinal variations of atmospheric density, the in-track uncertainty estimates must be adjusted accordingly ( $\sim 4$  km in this case). This scenario could also occur when there is a significant “a priori” in-track error in the input orbital model, as the latitude and longitude of the grazing point will contain additional uncertainty.

## 12 Concluding Remarks about Preliminary Simulations

The results of Part II help us better understand how confident we should be in the measurement of HCNM depending on our knowledge of a planet and the spacecraft’s orbital model during the horizon crossing. In order to evaluate the effects of uncertainty in atmospheric cross section and uncertainty in orbital velocity in Sections 7 and 8, we used a circular orbital model for the ISS on the day of NICER’s observation of the V4641 Sgr. horizon crossing, as well as the celestial coordinates of V4641 Sgr (which is  $2.59^\circ$  out of the orbital plane). Therefore, the specific results of this section are not completely generalizable, but provide a good estimate of the effects of error in orbital velocity and error in atmospheric cross section. Similar statements can be made about Sections 9, 10, and 11, as the results simply aim to provide a baseline estimate of the HCNM error budget.

1. For a satellite in a circular orbit around Earth with a linear velocity of 7.66 km/sec at an altitude of  $\sim 420$  km, the horizon crossing measurement will be shifted by  $\sim 1$  km when there is a 25 m/s error in orbital velocity and  $\sim 2$  km when there is 50 m/s error. The systematic shift forward or backward on the time axis is caused by incorrectly predicting the onset of transmittance data. Higher energies are slightly less effected by the error in orbital velocity (Section 7).
2. A 10% error in cross section causes a systematic in-track error of  $\sim 4$  km for the 1.0 – 2.0 keV energy band, but only  $\sim 2$  km for energy bands above 2.0 keV. This result makes sense because cross section changes most significantly below 2.0 keV (Section 8).
3. The effective transmittance model is important to predict the shape of the data below 3 keV, but it is not necessary for the higher energy bands.

4. The 1% Argon of Earth’s atmosphere is significant in the analysis of energy bands above Argon’s k-edge at 3.2 keV. Above 3.2 keV, Argon plays a more important role in X-ray absorption. (Section 9). The significance could be seen in the analysis of the Crab Nebula horizon crossing because of the Crab’s brightness in X-rays, but not in the results of the V4641 Sgr. crossing.
5. The latitude of a point on a telescope’s line of sight can be determined by either the complement of the “polar angle” formed with the z-axis of a planet-centered inertial frame or more precisely as the geodetic latitude if the exact shape of the planet is known. Latitude will always be known if a planet-centered inertial frame is defined. In order to determine the longitude, the rotation of the planet must be known and tracked. Although thermospheric density fluctuations with longitude are less extreme than changes in latitude, it is still important to know instantaneous longitude during a horizon crossing around Earth. For a planet with longitudinal variations in density similar to that of Earth, the lower energy X-rays that are transmitted at higher altitudes are more affected by not knowing the longitude of the telescopic graze point during a horizon crossing. (Section 11).

## Part III: Conclusions

The Horizon Crossing Navigational Method can locate the in-track position of a satellite by comparing a model transmittance curve to data collected by NICER. In Part I, the results of Table 5.3 show that the four energy bands from 1.0 – 5.0 keV locate the in-track position of the ISS to less than 3.4 km in the cool-start scenario. The weighted mean of these results, displayed in Table 5.6, gives extra weight to the energy bands that have more X-ray counts. The calculated position, as determined by the weighted mean of the results, is different from the “true” position by 0.92 km with an estimated uncertainty of 0.72 km. The estimated measurement uncertainty represents the amount of time for  $\chi^2$  to increase by one when sliding the model transmittance curve across the data. When using cross sections from Balucinska-Church and McCammon (1992) and an input orbital model with less uncertainty, weighted means agree at less than one standard error (Ruhl et al., 2022). Results of Table 5.6 show that when approximating the Earth as a sphere, the error in the in-track measurement increases to  $10.34 \pm 0.72$  km.

## 13 Final Words and Future Directions

In this paper, we have shown that a single horizon crossing can provide a highly precise in-track measurement of the satellite’s position in orbit. Additionally, we have shown how observing the same source over multiple orbits can provide an estimation of orbital period. Although a single horizon crossing can provide a highly accurate in-track measurement to a navigational filter, we imagine that horizon crossings will be of most importance when multiple can be observed within a single orbit, since the performance of a filter will improve with more measurements. If a spacecraft is able to conduct multiple sequential horizon crossings within an orbit, observing different sources in the sky, the horizon crossing measurements have the potential to be transformed (through coordinate transformations) into information about other elements of the satellite’s state vector, similar to how XNAV extracts three-dimensional navigational information by observing multiple pulsars (Sheikh et al., 2006). HCNM proves to be extremely promising for the future of autonomous, on-board space navigation, and can be used in conjunction with XNAV in order to better determine a spacecraft’s position and expand the reaches of X-ray navigation in space.

In this paper, we showed that HCNM measurement uncertainties are inversely proportional to the square root of the number of unattenuated counts analyzed (Figure 1.5). For sources brighter than the Crab Nebula, a horizon crossing can lead to measurements with standard errors of less than 300 meters. Future research includes identifying the best sources for HCNM, understanding how their angular extent affects the performance of HCNM, and determining how many horizon crossings could be achieved in a single orbit. There are many related questions that are necessary to understand when planning a horizon crossing, such as: what is the maximum orbital radius and maximum out-of-plane angle at which a satellite can observe a horizon crossing? How much knowledge of a planet’s terrain is necessary when conducting horizon crossings around

planets without atmospheres, such as the moon? Using this information in conjunction with an orbital trajectory and a catalogue of X-ray sources, such as the ROSAT All-Sky Survey, we can conduct realistic simulations of horizon crossings. There are multiple other technical considerations involved in planning a horizon crossing, some of which are specific to the telescope being used, and some of which are astrophysical consideration (Wood et al., 2020). Additionally, the thesis by Hladky (2022) considers factors involved in integrating HCNM into a deep space mission. Considering these technical and mission-design related questions are crucial before the implementation of HCNM in deep space navigation. There are also improvements on the scientific side of HCNM that will improve the accuracy of an HCNM measurement, enable a spacecraft to conduct horizon crossings around a larger number of planets, and enable the use a larger number of X-ray sources in the sky. Some of these scientific considerations are listed in the following sections.

### 13.1 Improvements to HCNM

In order to improve HCNM, a planet's atmospheric model can be made more robust and numerical methods can be modified to better take into account the absorption edges of atmospheric constituents. These modifications will enable us to predict transmittance curves across all possible energies emitted by the source's spectrum to the same high degree of accuracy. As will be discussed in Section 13.1.1, X-rays below 1 keV are much more difficult to model in Earth's atmosphere, and analysis of X-ray occultations is often restricted to energies above 0.6 keV. This range from 0.6 keV – 1.0 keV should also be utilized in HCNM, as many sources emit strongly in this bandpass. The energy range from 5.0 – 15.0 keV can also be utilized in order to use more data, and therefore, decrease the uncertainty in an HCNM measurement. In order to use higher energy X-ray data, we must understand where attenuation processes, other than absorption, start to occur in planetary atmospheres (likely  $\gtrsim 15$  keV).

Additionally, the simple atmospheric model used in this paper could be improved by considering the chemical make-up of Earth as a function of altitude. Results in this paper show that the simple mixing ratio of 78% N, 21% O, and 1% Ar works very well for Earth, but HCNM could likely produce even more accurate results if the make-up was a function of altitude. This extra factor in HCNM would be important in a scenario where HCNM is used to provide extremely high-precision in-track information, such as if it were used as an extra input to improve the performance of GPS. A more precise and generalizable atmospheric model will not only improve the in-track accuracy of HCNM, but it will also enable us to use a greater number of X-ray stars for horizon crossings (that emit in different energy ranges) and to navigate in different atmospheres around different planets. Furthermore, HCNM could also be generalized for elliptical orbits, as horizon crossings could be effective near the periape of an elliptical orbit. Although in this paper, information about radial position was determined by calculating an orbital period, the geometry of horizon crossings could possibly be used to determine an instantaneous orbital radius.

### 13.1.1 Use of X-ray Data Below 1 keV

If the equation of  $\sigma(E)$  for  $1.0 \leq E \leq 5.0$  keV is extrapolated below 1 keV (Equation (19)), thus smoothing over the k-edges of nitrogen and oxygen that occur at 0.40 keV and 0.53 keV respectively, our model produces an inaccurate transmittance curve. The model transmittance curve as compared to NICER data is shown in Figure 13.1 below, and if we continue our analysis, we find that  $t_{0,mkf} - t_{0,e} = 8.54$  seconds. The corresponding in-track error in  $\mathbf{r}_0$  comes out to  $\Delta r_e = 66.8$  km.

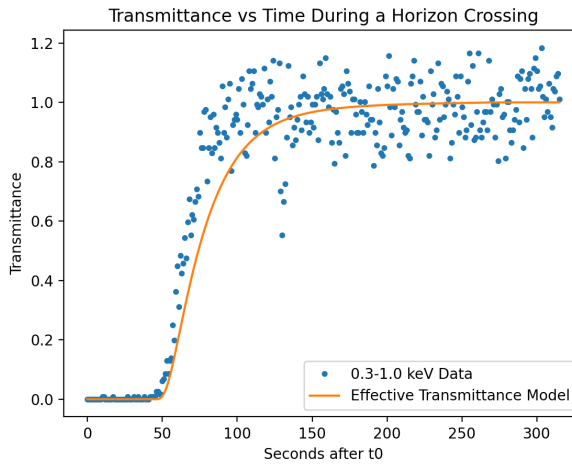


**Figure 13.1** Expected transmittance curve vs transmittance data as detected by NICER for the 0.3 - 1.0 keV energy band.

While the shape of the transmittance curve in Figure 13.1 is correctly determined by our probabilistic treatment of the source's spectrum and integration of atmospheric density along the line of sight, an incorrect coefficient of absorption cross section causes the transmittance model to be incorrectly shifted on the time axis. Moreover, since the extrapolated values of  $\sigma(E)$  below 1 keV are larger than the actual values of  $\sigma(E)$  for nitrogen and oxygen, we expect that the exponential function in Equation 17 would increase at a later time, thus producing a value of  $t_{0,e}$  that is smaller than  $t_{0,mkf}$  ( $t_{0,mkf} - t_{0,e} > 0$ ). Therefore, the expected curve would be shifted to the right since our model atmosphere absorbs more photons in the 0.3 - 1.0 keV than Earth's real atmosphere, which is exactly what we observe in Figure 13.1. Figure 13.2 below shows a plot of the photo-electric cross sections of nitrogen, oxygen, and argon (Balucinska-Church and McCammon, 1992).

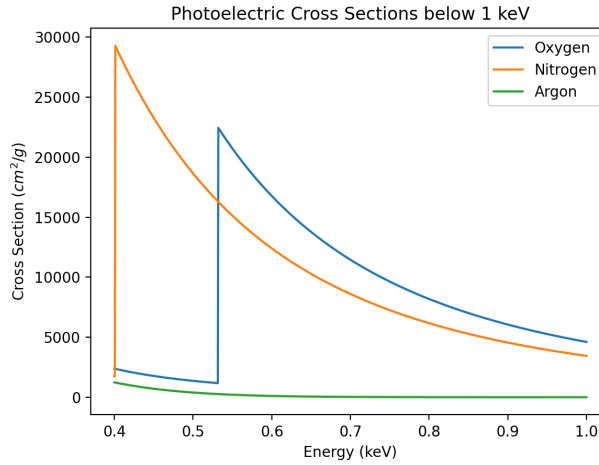


**Figure 13.2** Photoelectric cross sections of Earth's major atmospheric constituent (Balucinska-Church and McCammon, 1992)

## 13.2 Use of the C Statistic

An alternative maximum likelihood estimator to  $\chi^2$ , the C-statistic, has the potential to identify when the shape of the transmittance model is not consistent with the shape of the data points. Determan et al. (2007) used the C-statistic in their method of XOS in order to further address the Poisson-nature of X-ray data, and they note that the C Statistic provides additional benefits over  $\chi^2$ , especially at low signal-to-noise ratios. The C statistic, which was introduced by Cash (1979), is given by

$$C = -2 \sum_i \left[ \left( O_i \cdot \ln \left( \frac{O_i}{E_i} \right) + E_i - O_i \right) \right] \quad (43)$$

where  $O_i$  is the measured data and  $E_i$  is the model estimate for the  $i$ th point.

We noticed that the C statistic does not converge for the 3.0 – 4.0 keV and 4.0 – 5.0 keV energy bands when comparing the two curves when the model is calculated with certain assumptions. Specifically, the C-statistic diverged for these energy bands when using the circular orbit model as well as the spherical Earth approximation. Therefore, while  $\chi^2$  will always converge when comparing the data to the model, the C-statistic will not always converge. In this way, divergence of the C-statistic provides insight into the quality of the curve comparison. In future research, we should consider calculating the C statistic (in addition to  $\chi^2$ ) as an error-handling device. Divergence of the C statistic could indicate that an assumption used in the calculation of the model transmittance curve may be inaccurate and may affect the reliability of the HCNM measurement. On-board a spacecraft, especially in a deep space navigation scenario, an error-handling method like this would be extremely valuable.

## 14 References

- [1] Balucinska-Church, M. and McCammon, D. Photoelectric absorption cross sections with variable abundances. *The Astrophysical Journal*, 400:699, 1992. doi: 10.1086/172032.
- [2] Bate, R. R., Mueller, D. D., White, J. E., and Saylor, W. W. *Fundamentals of Astrodynamics*. Dover Publications, Inc., Mineola, New York, 2020.
- [3] Berger, M. J. and Hubbell, J. Xcom: Photon cross sections on a personal computer. Technical report, National Bureau of Standards, Washington, DC. Center for Radiation, 1987.
- [4] Cash, W. Parameter estimation in astronomy through application of the likelihood ratio. *The Astrophysical Journal*, 228:939–947, 1979.
- [5] Lynch, J. R. Geodetic coordinate conversions. *Geodetic to/from Geocentric Latitude. Available online: <http://lynchhg3c.com/Technote/geodesy/coordcvt.pdf>*, 2006.
- [6] Curtis, H. D. *Orbital Mechanics for Engineering Students*. Embry-Riddle Aeronautical University, Daytona Beach, Florida, 2005.
- [7] Determan, J. R., Budzien, S. A., Kowalski, M. P., Lovellette, M. N., Ray, P. S., Wolff, M. T., Wood, K. S., Titarchuk, L., and Bandyopadhyay, R. Measuring atmospheric density with X-ray occultation sounding. *Journal of Geophysical Research (Space Physics)*, 112(A6):A06323, June 2007. doi: 10.1029/2006JA012014.
- [8] Emadzadeh, A. A. and Speyer, J. L. *Navigation in Space by X-ray Pulsars*. Springer Science & Business Media, 2011.
- [9] Gendreau, K. C., Arzoumanian, Z., Adkins, P. W., Albert, C. L., Anders, J. F., Aylward, A. T., Baker, C. L., Balsamo, E. R., Bamford, W. A., Benegalrao, S. S., et al. The neutron star interior composition explorer (nicer): design and development. In *Space telescopes and instrumentation 2016: Ultraviolet to gamma ray*, volume 9905, page 99051H. International Society for Optics and Photonics, 2016. doi: 10.1117/12.2231718.
- [10] Hladky, R. M. Designing a deep space mission with autonomous x-ray navigation. Bachelor's thesis, Haverford College, 370 Lancaster Ave, Haverford, PA 19041, May 2022.
- [11] Katsuda, S., Fujiwara, H., Ishisaki, Y., Yoshitomo, M., Mori, K., Motizuki, Y., Sato, K., Tashiro, M. S., and Terada, Y. New measurement of the vertical atmospheric density profile from occultations of the crab nebula with x-ray astronomy satellites suzaku and hitomi. *Journal of Geophysical Research: Space Physics*, 126(4), 2021.
- [12] Macomber, M. M. World geodetic system 1984. Technical report, Defense Mapping Agency, Washington, DC, 1984.

- 
- [13] Matzka, J., Stolle, C., Yamazaki, Y., Bronkalla, O., and Morschhauser, A. The geomagnetic  $K_p$  index and derived indices of geomagnetic activity. *Space Weather*, 19(5):e2020SW002641, 2021.
  - [14] Mitchell, J. W., Winternitz, L. B., Hassouneh, M. A., Price, S. R., Semper, S. R., Yu, W. H., Ray, P. S., Wolf, M. T., Kerr, M., Wood, K. S., et al. Sextant x-ray pulsar navigation demonstration: initial on-orbit results. In *Proceedings of the AAS Guidance, Navigation, and Control Conference, Paper AAS 18-155*, 2018.
  - [15] Picone, J. M., Hedin, A. E., Drob, D. P., and Aikin, A. C. NRLMSISE-00 empirical model of the atmosphere: Statistical comparisons and scientific issues. *Journal of Geophysical Research (Space Physics)*, 107(A12):1468, December 2002. doi: 10.1029/2002JA009430.
  - [16] Qian, L. and Solomon, S. C. Thermospheric density: An overview of temporal and spatial variations. *Space science reviews*, 168(1):147–173, 2012.
  - [17] Ray, P. S., Sheikh, S. I., Graven, P. H., Wolff, M. T., Wood, K. S., and Gendreau, K. C. Deep space navigation using celestial x-ray sources. In *Proceedings of the 2008 National Technical Meeting of The Institute of Navigation*, pages 101–109, 2008.
  - [18] Roble, R. G. and Hays, P. A technique for recovering the vertical number density profile of atmospheric gases from planetary occultation data. *Planetary and Space Science*, 20(10):1727–1744, 1972.
  - [19] Ruhl, N. C., Lommen, A. N., Schwab, N. H., Hladky, R. M., Wood, K. S., and Ray, P. S. Use of x-ray star horizon crossings to enhance performance of x-ray navigation. *Proceedings of the AAS Guidance, Navigation, and Control Conference, Paper AAS 22-073*, 2022.
  - [20] Schwab, N. H. Simulating horizon crossings events for satellite navigation. Bachelor’s thesis, Haverford College, 370 Lancaster Ave, Haverford, PA 19041, May 2022.
  - [21] Sheikh, S. I., Pines, D. J., Ray, P. S., Wood, K. S., Lovellette, M. N., and Wolff, M. T. Spacecraft navigation using x-ray pulsars. *Journal of Guidance, Control, and Dynamics*, 29(1):49–63, 2006. doi: 10.2514/1.13331.
  - [22] Winternitz, L. M., Gendreau, K. C., Hassouneh, M., Mitchell, J. W., Fong, W. H., Lee, W.-T., Gavriil, F., and Arzoumanian, Z. The role of x-rays in future space navigation and communication. In *Proceedings of the AAS Guidance, Navigation, and Control Conference, Paper AAS 13-082*, 2013.
  - [23] Wood, K. S. Navigation studies utilizing the NRL-801 experiment and the ARGOS satellite. In *Small Satellite Technology and Applications III*, volume 1940 of *Society of Photo-Optical Instrumentation Engineers (SPIE) Conference Series*, pages 105–116, September 1993. doi: 10.1117/12.156637.

- [24] Wood, K. S. and Ray, P. S. The NRL Program in X-ray Navigation. *arXiv e-prints*, December 2017. doi: arXiv:1712.03832.
- [25] Wood, K. S., Determan, J. R., Ray, P. S., Wolff, M. T., Budzien, S. A., Lovellette, M. N., and Titarchuk, L. Using the unconventional stellar aspect (USA) experiment on ARGOS to determine atmospheric parameters by x-ray occultation. In Larar, A. M. and Mlynczak, M. G., editors, *Optical Spectroscopic Techniques, Remote Sensing, and Instrumentation for Atmospheric and Space Research IV*, volume 4485 of *Society of Photo-Optical Instrumentation Engineers (SPIE) Conference Series*, pages 258–265, January 2002. doi: 10.1117/12.454259.
- [26] Wood, K. S., Ray, P. S., Wolff, M. T., and Gendreau, K. Satellite navigation using x-ray pulsars and horizon crossings of x-ray stars. In *Proceedings of the AAS Guidance, Navigation, and Control Conference, Paper AAS 20-124*, 2020.

## A Additional HCNM Results

Energy Band	1.0 – 2.0 keV	2.0 – 3.0 keV	3.0 – 4.0 keV	4.0 – 5.0 keV
$\Delta t_{hc} \pm \delta t_{hc}$ (sec)	$0.02 \pm 0.14$	$0.11 \pm 0.20$	$0.27 \pm 0.27$	$0.02 \pm 0.38$
$\Delta r_{hc} \pm \delta r_{hc}$ (km)	$0.15 \pm 1.09$	$0.84 \pm 1.54$	$2.07 \pm 2.09$	$0.15 \pm 2.90$
Unattenuated Counts, $N_0$	244	89	40	19

**Table A.1** Results from the horizon crossing of V4641 Sgr using the “mkf” orbital solution as the input model, an ellipsoidal Earth, and BCMC cross sections.  $\Delta t_{hc}$  is the error in correctly identifying  $t_{0,mkf}$ , the time at which the spacecraft is at the position  $\mathbf{r}_{0,mkf}$ .  $\Delta r_{hc}$  is the in-track error corresponding to  $\Delta t_{hc}$ . The uncertainties  $\delta t_{hc}$  and  $\delta r_{hc}$  are related to the number of attenuated counts in a given energy band. This table is re-printed from Ruhl et al. (19).

Energy Band	1.0 – 2.0 keV	2.0 – 3.0 keV	3.0 – 4.0 keV	4.0 – 5.0 keV
$\Delta t_{hc} \pm \delta t_{hc}$ (sec)	$0.11 \pm 0.14$	$0.19 \pm 0.18$	$0.32 \pm 0.24$	$0.10 \pm 0.38$
$\Delta r_{hc} \pm \delta r_{hc}$ (km)	$0.84 \pm 1.07$	$1.46 \pm 1.37$	$2.45 \pm 1.84$	$0.77 \pm 2.94$
Unattenuated Counts, $N_0$	244	89	40	19

**Table A.2** Results from the horizon crossing of V4641 Sgr. using a circular orbit model, an ellipsoidal Earth, and BCMC cross sections. This table can directly be compared to Table A.1 in order to see the effect of an input orbit model that is not exact.

Energy Band	1.0 – 2.0 keV	2.0 – 3.0 keV	3.0 – 4.0 keV	4.0 – 5.0 keV
Time Range	44.0 – 98.0 sec	41.0 – 76.0 sec	41.0 – 65.0 sec	41.0 – 58.0 sec
Transmittance Range	1.0% – 99.0%	3.8% – 99.0%	25.6% – 99.0%	51.6% – 99.0%
$\Delta t_{hc} \pm \delta t_{hc}$ (sec)	$0.01 \pm 0.03$	$0.04 \pm 0.05$	$-0.24 \pm 0.10$	$-0.01 \pm 0.25$
$\Delta r_{hc} \pm \delta r_{hc}$ (km)	$0.08 \pm 0.20$	$0.31 \pm 0.40$	$-1.84 \pm 0.77$	$-0.08 \pm 1.88$

**Table A.3** Results for the horizon crossing of the Crab Nebula when comparing only the portions of the data when NICER is confidently locked-on. The results are calculated using the “mkf” orbital solution as the input model, an ellipsoidal Earth, and BCMC cross sections. This table is re-printed from Ruhl et al. (19).

## B Inputs to the NRLMSISE-00 Density Model

We access the NRLMSISE-00 atmospheric model through “pymsis”, a python wrapper for the MSIS model, created by Greg Lucas and the University of Colorado Space Weather Technology,

Research and Education Center (SWx TREC). Table B.1 shows the inputs to NRLMSISE-00 when extracting the density profiles used in this paper.

Observation	$t_{0,mkf}$ (UTC)	Lat. of gp	Lon. of gp	F10.7 (sfu)	Ap
V4641 Sgr	2020-02-03 19:39:27.25	$-43.26^\circ$	$90.28^\circ$	69.7	12
Crab Nebula	2021-08-11 16:31:19.01	$-43.91^\circ$	$168.69^\circ$	75.2	2

**Table B.1** Inputs to the MSISE-00 atmospheric model to extract profiles of density as a function of altitude. Longitude and Latitude correspond to the “graze point” (gp), the point on the telescopic line of sight where tangent altitude equals zero, which is shown in Figure 3.1. Geomagnetic Ap indices are provided by GFZ German Research Centre for Geosciences(13). The f10.7 cm solar flux is provided by Space Weather Canada (1 sfu =  $10^4$ Jy).

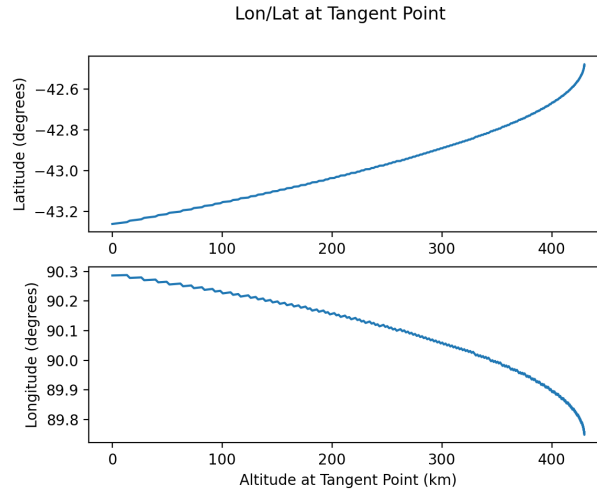


**Figure 2.1** Latitude and longitude of tangent point during the crossing of V4641 Sgr. Since the latitude and longitude of the tangent point do not change much throughout the horizon crossing, we use a single density profile as a function of altitude calculated at the grazing point (gp).

## C Additional Information

Observation	Source RA	Source DEC	Source $\psi$	Lat. ISS	Lon. ISS	Alt. ISS
V4641 Sgr	$274.839^\circ$	$-25.407^\circ$	$-2.59^\circ$	$-29.53^\circ$	$71.47^\circ$	424.27 km
Crab Nebula	$83.633^\circ$	$22.014^\circ$	$2.06^\circ$	$-51.38^\circ$	$139.92^\circ$	436.72 km

**Table C.1** Right ascension, declination, and out-of orbital plane angle ( $\psi$ ) of the black hole binary V4641 Sgr and the Crab Nebula. The position of the ISS at the start of the horizon crossing,  $\mathbf{r}_{0,mkf}$ , is given in terms of latitude, longitude, and altitude.

## D Additional Figures

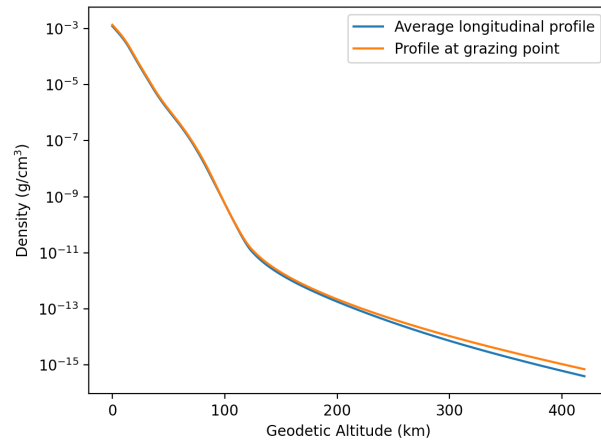


**Figure 4.1** Comparison of the exact density profile and the longitudinally-averaged density profiles used in Section 11.

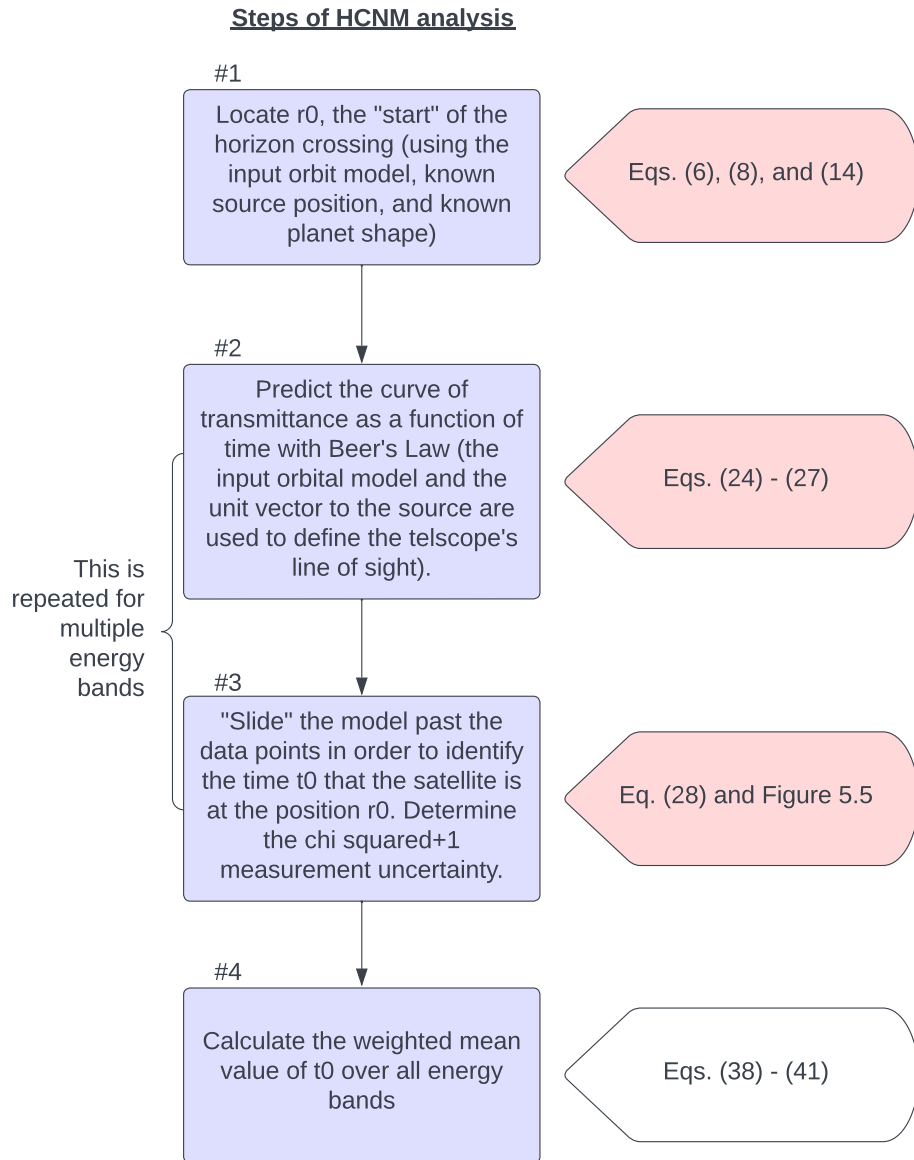


**Figure 4.2** Summary of the four main steps involved in an HCNM measurement. This diagram starts by assuming that the input orbital model is already defined, but it can also be defined from the “cool start” formulation described in Part II.

## E Table of Symbols

Symbol	Description	Location in Text
<b>Orbital Description</b>		
$\{\hat{\mathbf{x}}, \hat{\mathbf{y}}, \hat{\mathbf{z}}\}$	Planet-centered inertial coordinate frame	Section 2
$\{\hat{\mathbf{p}}, \hat{\mathbf{q}}, \hat{\mathbf{w}}\}$	Perifocal reference frame	Figure 3.5
$\hat{\mathbf{h}}$	Pole of orbit unit vector	Section 2
$\hat{\mathbf{n}}$	Line of nodes unit vector	Equation 3
$e, \omega_p, i, \Omega$	Known keplerian orbital elements	Equation 4
$T_{\text{guess}}, T_{\text{best}}, \omega$	Calculated orbital period and angular velocity of the model orbit	Section 5.3.1
$R_{\text{orbit}}$	Radius of model orbit calculated from $T_{\text{best}}$	Equation 21
<b>Geometry For a Specific Celestial Source and Orbit</b>		
$\hat{\mathbf{s}}$	Unit position vector of source	Section 3
$\psi$	Out-of-plane angle of source	Equation 7
$\hat{\mathbf{s}}_{\text{proj}}$	Position vector of source, projected onto orbit plane and normalized	Equation 5
$\hat{\mathbf{g}}$	“Grazing” unit vector towards the line of sight’s tangent point	Section 3
$\hat{\mathbf{g}}_{\text{proj}}$	“Grazing” unit vector, projected into the orbital plane	Section 3
$\mathbf{r}_{0,2d}$	Initial estimate of satellite’s location at the start-of-crossing	Equation 6
$\mathbf{r}_{\text{s}}$	Parametric equation of the tangent line of sight	Equation 12
<b>Atmospheric Model</b>		
$T$	Transmittance of photons as received by the telescope	Equation 17
$\sigma(E)$	Absorption cross section ( $\text{cm}^2/\text{g}$ ) as a function of photon energy	Section 4
$\rho(z)$	Density ( $\text{g}/\text{cm}^3$ ) as a function of altitude above sea level	Section 4
$\tau$	Non-dimensional optical depth	Equation 18
$C_n$	Mixing ratio of atmospheric constituent $n$	Section 4
$a, b, c, \phi, \theta$	Parameters in the Oblate Earth Model	Section 5.2
<b>Results and Error Analysis</b>		
$\mathbf{r}_{0,\text{mkf}}$	“Exact” position of satellite at crossing	Section 5.4
$t_{0,\text{mkf}}$	“Exact” time of satellite at crossing	Section 5.4
$\mathbf{r}_{0,\text{hc}} (\mathbf{r}_{0,3d})$	Expected location of the satellite at start-of-crossing	Equations 12, 14
$t_{0,e}$	Calculated time of crossing, specific to each energy band	Section 5.3.3
$\theta_{0,hc}, \theta_{0,mkf}$	In-track anomaly of $\mathbf{r}_{0,\text{hc}}$ and $\mathbf{r}_{0,\text{mkf}}$	Equation 33
$\Delta\theta_{\text{circ}}$	Difference in in-track positions of $\mathbf{r}_{0,\text{hc}}$ and $\mathbf{r}_{0,\text{mkf}}$	Equation 32
$\Delta r_{\text{circ}}$	Total geometrical error between $\mathbf{r}_{0,\text{hc}}$ and $\mathbf{r}_{0,\text{mkf}}$	Equation 29
$\Delta\theta_e$	In-track angular displacement resulting from $t_{0,e} \neq t_{0,mkf}$	Equation 35
$\Delta r_e$	In-track error resulting from $\Delta\theta_e$	Equation 34
$\mathbf{r}_{0,e}$	Position of satellite in model orbit at $t_{0,\text{mkf}}$	Equation 37
$\Delta r_{\text{tot}}$	Total difference between predicted and real position at $t_{0,\text{mkf}}$	Equation 36

**Table E.1** Table of symbols used in the Horizon Crossing Navigational Method (HCNM)